



Disk and Envelope Streamers of the GGD 27-MM1 Massive Protostar

M. Fernández-López¹ , J. M. Girart^{2,3} , J. A. López-Vázquez⁴ , R. Estalella^{5,6} , G. Busquet^{3,5,6} , S. Curiel⁷ , and N. Añez-López⁸

¹Instituto Argentino de Radioastronomía (CCT-La Plata, CONICET; CICPBA), C.C. No. 5, 1894, Villa Elisa, Buenos Aires, Argentina; manferna@gmail.com

²Institut de Ciències de l'Espai (ICE-CSIC), Campus UAB, Carrer de Can Magrans S/N, E-08193 Cerdanyola del Valles, Catalonia

³Institut d'Estudis Espacials de Catalunya (IEEC), c/ Gran Capità, 2-4, E-08034 Barcelona, Spain

⁴Academia Sinica Institute of Astronomy and Astrophysics, No. 1, Section 4, Roosevelt Road, Taipei 10617, Taiwan

⁵Departament de Física Quàntica i Astrofísica (FQA), Universitat de Barcelona (UB), c/ Martí i Franquès 1, E-08028 Barcelona, Spain

⁶Institut de Ciències del Cosmos (ICCUB), Universitat de Barcelona (UB), c/ Martí i Franquès 1, E-08028 Barcelona, Spain

⁷Instituto de Astronomía, Universidad Nacional Autónoma de México (UNAM), Apartado Postal 70-264, DF 04510, México

⁸Université Paris-Saclay, Université Paris Cité, CEA, CNRS, AIM, F-91191, Gif-sur-Yvette, France

Received 2022 December 22; revised 2023 July 12; accepted 2023 July 12; published 2023 October 10

Abstract

We present new Atacama Large Millimeter/submillimeter Array 0.98 mm observations of the continuum emission and several molecular lines toward the high-mass protostellar system GGD 27-MM1, driving the HH 80-81 radio jet. The detailed analysis of the continuum and the CH₃CN molecular emission allows us to separate the contributions from the dust content of the disk (extending up to 190 au), the molecular content of the disk (extending from 140–360 au), and the content of the envelope, revealing the presence of several possible accretion streamers (also seen in other molecular tracers, such as CH₃OH). We analyze the physical properties of the system, producing temperature and column density maps, and radial profiles for the disk and the envelope. We qualitatively reproduce the trajectories and line-of-sight velocities of the possible streamers using a theoretical model approach. An ad hoc model of a flared disk comprising a hot dust disk embedded in cold gas fits the H₂S emission, which revealed the molecular disk as a crescent shape with a prominent central absorption. Another fit to the central absorption spectrum suggests that the absorption is probably caused by different external cold layers from the envelope or the accretion streamers. Finally, the analysis of the rotation pattern of the different molecular transitions in the molecular disk suggests that there is an inner zone devoid of molecular content.

Unified Astronomy Thesaurus concepts: [Interstellar molecules \(849\)](#); [Young stellar objects \(1834\)](#); [Protostars \(1302\)](#); [Interstellar medium \(847\)](#)

1. Introduction

The presence of rotationally supported disks around low-mass young stellar objects (YSOs) appears to be almost ubiquitous. The disks' timescales are about a few million years, large enough to be considered planet-forming disks (Haisch et al. 2001). Recent Atacama Large Millimeter/submillimeter Array (ALMA) observations have allowed a significant advance in the understanding of the properties of these disks and their evolution (e.g., Andrews 2020; Öberg et al. 2021).

Because of their typically shorter timescales, larger distances, and large obscuration, the properties of the disks around massive stars, as well as their evolution, are less known. There are many large, ~ 1000 au, disk-like structures with clear velocities gradients (e.g., Sánchez-Monge et al. 2013; Cesaroni et al. 2017; Beuther et al. 2017; Tanaka et al. 2020; Williams et al. 2022). Smaller disks are, however, more difficult to find (e.g., Ilee et al. 2018; Maud et al. 2019), but they are usually very massive ($2\text{--}5 M_{\odot}$) and hot ($\gtrsim 400$ K). The closest case of a disk around a massive star, Orion I, has peculiar features such as its SiO maser emission and its association with an explosive outflow (Plambeck & Wright 2016; Hirota et al. 2017; Ginsburg et al. 2019; Wright et al. 2022), only found in a handful of sources (Guzmán Ccolque et al. 2022) and it probably cannot be considered as a reference case. The rapid

evolution of massive stars, makes the disk become fully ionized in relatively short timescales (e.g., Jiménez-Serra et al. 2020).

The traditional view is that rotationally supported disks are fed by infalling, relatively flattened envelopes. In this scenario, the envelope can be understood as the expected pseudo-disk in the classical theoretical picture of unstable magnetized cloud cores (Galli & Shu 1993). However, recent observations show that accretion toward disks around low-mass YSOs is probably significantly asymmetric along all their evolutionary stages (Alves et al. 2019; Yen et al. 2019; Le Gouellec et al. 2019; Alves et al. 2020; Pineda et al. 2020; Huang et al. 2020, 2021; Grant et al. 2021; Garufi et al. 2022; Murillo et al. 2022; Thieme et al. 2022; Pineda et al. 2023; Pinte et al. 2023). This transforms the steady and more static view of the accretion process into a more dynamic and chaotic scenario.

The massive star driving the highly collimated jet associated with HH 80-81 (e.g., Rodríguez & Reipurth 1989; Martí et al. 1993; Masqué et al. 2012, 2015), is one of these protostellar systems surrounded by a relatively compact, very massive and hot disk, associated with the millimeter source GGD 27-MM1 (Girart et al. 2018). The emission can well be fitted by scale-up versions of accretion disk models around low-mass young stars (Añez-López et al. 2020). This allowed us to constrain the disk radius, $\simeq 170$ au, the stellar mass, $\simeq 20 M_{\odot}$, and the disk mass, $\simeq 5 M_{\odot}$ (assuming a distance of 1.4 kpc, see Añez-López et al. 2020). It has also allowed us to theoretically derive the density and temperature radial and vertical profiles of the disk (Añez-López et al. 2020). The dusty disk is surrounded by a bright molecular, disk-like structure with a radius of ~ 1000 au, which is also perpendicular to



Original content from this work may be used under the terms of the [Creative Commons Attribution 4.0 licence](#). Any further distribution of this work must maintain attribution to the author(s) and the title of the work, journal citation and DOI.

the radio jet (Gómez et al. 2003; Fernández-López et al. 2011a, 2011b; Carrasco-González et al. 2012; Girart et al. 2017). The presence of a rotating disk perpendicular to a highly collimated jet suggests that at least some massive stars form similarly to their lower mass counterparts, but with a more vigorous and in a significantly more energetic scale (Heathcote et al. 1998; Molinari et al. 2001; Carrasco-González et al. 2010; Rodríguez-Kamenetzky et al. 2017, 2019).

In this work, we present new continuum and molecular line observations taken with ALMA telescope toward the GGD 27-MM1 protostellar system. A description of the observations is provided in Section 2. Section 3 describes the continuum and molecular diversity content of the system, and Section 4 presents a detailed analysis of its physical properties from studying the molecular emission in the disk, the envelope, and an ensemble of possible streamers reported in the system for the first time. In Section 5, we discuss the results of the analysis and in Section 6 we summarize the main conclusions of this contribution.

2. Observations

We performed ALMA Cycle 4 observations (project 2015.1.00480.S) taken at Band 7 in GGD 27. These observations comprised two tracks carried out on 2016 September 6 and 7. Both used 39 antennas for a total on-source integration time of 60.7 minutes. The baselines ranged between 15.1 and 2500 m. The weather conditions reported at the ALMA site during the observations indicated a precipitable water column of 0.5 and 0.6 mm for the two tracks respectively, with about 1.1 airmass for both. The median T_{sys} ranged from 80–120 K at the observing frequency. The phase center was placed at $(\alpha, \delta)_{J2000} = (18^{\text{h}}19^{\text{m}}12^{\text{s}}.101, -20^{\circ}47'30''.984)$, and the primary beam of the 12 m antennas is $19''$.

The correlator setup included four spectral windows (two in each sideband) centered at 298.923 GHz (spw25), 300.435 GHz (spw27), 309.715 GHz (spw31), and 312.853 GHz (spw29). The spectral resolution was 0.5 km s^{-1} for spw27 and spw31, and 1.0 km s^{-1} for spw25 and spw29. The total continuum bandwidth was about 3.750 GHz and 2.320 GHz before and after spectral line removal, respectively.

The data were calibrated following the standard pipeline procedures inside the CASA package (McMullin et al. 2007, version 4.7.0-1). J1924-2914 was used as flux and bandpass calibrator, while J1832-2039 was used as phase calibrator. We set the flux of J1924-2914 at 298.923 GHz to 3.431 Jy, and we assume its spectral index to be -0.595 .⁹ After setting J1924-2914 data amplitudes to this flux scale, and applying the correction to all the data, we obtained a flux for J1832-2039 of $303 \pm 4 \text{ mJy}$ at 298.923 GHz for track 1 and $312 \pm 2 \text{ mJy}$ for track 2.

We constructed a continuum line-free data set using a Briggs weighting with $\text{robust} = 0.5$. We made three self-calibration iterations, which improved the signal-to-noise ratio of the continuum image. The final continuum image has an rms of $0.14 \text{ mJy beam}^{-1}$ and a synthesized beam of $0''.14 \times 0''.11$ (P.A. = 61°). Then, the self-calibration solutions were applied to the spectral windows. In this work, we only analyzed a few spectral lines detected in these observations (see Table 1). The rest of the lines will be presented in a forthcoming contribution.

⁹ The flux and spectral index of this quasar were provided with the pipeline and extracted from the ALMA flux monitoring of quasars. The spectral index is defined here as α , with $S_{\nu} \propto \nu^{\alpha}$.

3. Results

3.1. The GGD 27-MM1 Disk and Envelope System: Continuum Emission

Figure 1 shows the dust continuum emission at 0.98 mm (306.1 GHz) toward GGD 27-MM1, as observed with ALMA. The emission is dominated by a compact component, slightly elongated roughly along the east–west direction, surrounded by a tenuous emission, also elongated in the same direction, that extends in total about $1''$ (1400 au at the source distance). Within the tenuous component, there are two peaks of emission toward the northwest and northeast with respect to the continuum peak. These two peaks are not present in the images built up using only long baselines (Girart et al. 2018). From Girart et al. (2018) and Añez-López et al. (2020) we know that there is an unresolved (with a radius of $\lesssim 6 \text{ au}$) continuum source at the very center of the system with a spectral index of $\simeq 1.2$ (see Section 7.1 of Añez-López et al. 2020). The nature of this source is still unknown. For instance, it could be due to an extremely compact ionized HII region, or to the basis of the thermal radio jet. By extrapolating its contribution at the observing frequency and using a spectral index of 1.2, we estimate its flux intensity to be 23 mJy beam^{-1} . We modeled the 0.98 mm continuum emission assuming that the following components have a 2D-Gaussian profile: (i) an unresolved source, (ii) a disk, (iii) the envelope, (iv) an unresolved NE component, and (v) an NW compact component. We used the peak intensity and position of each component as initial guess values. For the first three components, we used the intensity and position of the continuum peak. For the central source (i), we fixed the peak intensity with a value of 23 mJy beam^{-1} and a size consistent with an unresolved pointlike source. We also assumed that the NE compact component is unresolved. We fixed the position of the compact and the NW components. The rest of the parameters for all the components were treated as free parameters. We used the CASA task *imfit* to do the fitting. Table 2 shows the results. A visualization of the fit can be found in Appendix A. We note that the values of the fit for the envelope and of the disk may not be unique and there may be some degeneracy, especially in the flux density. The disk’s radius, 133 mas (about 190 au) is slightly smaller than the value derived by Girart et al. (2018) and Busquet et al. (2019), 170 mas (240 au), from higher angular resolution 1.14 mm ALMA observations. Interestingly, the value obtained by fitting the 1.14 mm emission using the α -viscosity disk model (Añez-López et al. 2020) was 170 au. The values of the position angle, $\simeq 113^{\circ}$, and of the minor-to-major axis ratio, $\simeq 0.68$ (i.e., a line-of-sight disk inclination of $\simeq 42^{\circ}$), are similar to those previously reported. The envelope is also elongated approximately in the same direction as the disk (the difference is small: $\simeq 5^{\circ}$). Both structures also have the same axis ratio. The NW dusty component appears to be elongated roughly along the north–south direction, and has a major axis length of $0''.26$ (360 au). The total flux from all the components in MM1 (compact object, disk, and envelope) is 816 mJy, while the flux from the residual map at the location of the sources is 3 mJy. If we compare this value with the value obtained with the Submillimeter Array at 1.36 mm at an angular resolution of $\sim 0''.5$ (with this angular resolution, all three components would be barely resolved), $441 \pm 6 \text{ mJy}$ Fernández-López et al. (2011a), then the overall spectral index is ~ 1.9 . This spectral index is in agreement with the previous measurements toward this source (Fernández-López et al. 2011a).

Table 3 contains information about the mass and column density of the different dusty components. As a rough approximation, we

Table 1
Spectral Lines

Transition	ν_{rest} (GHz)	E_{up} (K)	$\log_{10}(A_{ij})$ ($\log_{10}(\text{s}^{-1})$)	Synthesized Beam		$\delta\nu$ (km s^{-1})	rms (mJy beam^{-1})
				(arcsec \times arcsec)	(deg)		
CH ₃ CN 17 ₀ -16 ₀	312.687743	135.1	-2.73710	0".17 \times 0".13	77.3	0.9	1.9
CH ₃ CN 17 ₁ -16 ₁	312.681731	142.2	-2.73867	0".17 \times 0".13	77.3	0.9	1.9
CH ₃ CN 17 ₂ -16 ₂	312.663699	163.6	-2.74327	0".17 \times 0".13	77.3	0.9	1.9
CH ₃ CN 17 ₃ -16 ₃	312.633653	199.4	-2.75105	0".17 \times 0".13	77.3	0.9	1.9
CH ₃ CN 17 ₄ -16 ₄	312.591607	249.3	-2.76222	0".17 \times 0".13	77.3	0.9	1.9
CH ₃ CN 17 ₅ -16 ₅	312.537576	313.6	-2.77699	0".17 \times 0".13	77.3	0.9	1.9
CH ₃ CN 17 ₆ -16 ₆	312.471584	392.1	-2.79579	0".17 \times 0".13	77.3	0.9	1.9
CH ₃ CN 17 ₇ -16 ₇	312.393656	484.8	-2.81905	0".17 \times 0".13	77.3	0.9	1.9
CH ₃ CN 17 ₈ -16 ₈	312.303825	591.7	-2.84738	0".17 \times 0".13	77.3	0.9	1.9
CH ₃ CN 17 ₉ -16 ₉	312.202126	712.8	-2.88193	0".17 \times 0".13	77.3	0.9	1.9
SO ₂ 9 _{2,8} -8 _{1,7}	298.576307	51.0	-3.84092	0".19 \times 0".14	88.2	1.0	1.5
SO ₂ 12 _{6,6} -13 _{5,9}	312.258421	160.0	-4.38674	0".16 \times 0".13	77.0	1.0	1.6
SO ₂ 19 _{3,17} -19 _{2,18}	299.316816	197.0	-3.69102	0".17 \times 0".14	78.5	1.0	1.4
SO ₂ 32 _{3,29} -32 _{2,30}	300.273416	518.7	-3.59400	0".18 \times 0".13	79.1	0.5	1.7
SO ₂ 33 _{10,24} -34 _{9,25}	310.017205	760.5	-4.21948	0".16 \times 0".13	76.8	0.5	1.8
CH ₃ OH 3 _{1,2} -2 _{0,2}	310.192994	35.0	-4.05554	0".17 \times 0".13	76.8	0.5	1.8
H ₂ CO 4 _{1,3} -3 _{1,2}	300.836635	47.9	-3.14420	0".18 \times 0".13	80.0	0.5	1.8
H ₂ S 3 _{3,0} -3 _{2,1}	300.505560	168.9	-3.98895	0".18 \times 0".13	79.2	0.5	1.9
HC ₃ N 33-32	300.159647	244.9	-2.66753	0".18 \times 0".13	79.1	0.5	1.7

Note. The quoted rest frequencies have been extracted from the Molecular Spectroscopy database of the Jet Propulsion Laboratory (JPL) using the online port Splatalogue (Remijan et al. 2007) at <https://splatalogue.online/index.php>.

assumed that the dust emission in the envelope is optically thin and isothermal, despite we know that the temperature progressively decreases with distance to the center (see Section 4.1). We also used a gas-to-dust ratio of 100, a dust opacity of $1.0 \text{ cm}^2 \text{ g}^{-1}$ at 1.3 mm appropriate for dust with thin ice mantles (Ossenkopf & Henning 1994), which we extrapolate to the observing wavelength using an opacity spectral index with an exponent $\beta = 1.6$, typical of interstellar medium grains (Draine 2006), and the 306 GHz flux extracted in this work. Finally, we considered a range of dust temperatures for the envelope; we assumed that the temperature of the envelope may be between 110 and 150 K (see Section 4.1 and Fernández-López et al. 2011a). Hence, we derived an envelope mass of $\sim 0.22 M_{\odot}$ and a column density of $9\text{--}12 \times 10^{22} \text{ cm}^{-2}$. Likewise, we also estimate the mass of the NE and NW components (about 0.005 and 0.01 M_{\odot} , respectively). For their temperature, we assume they are at a similar temperature as the rest of the envelope. However, the NE component is at a position where the CH₃CN analysis (see Section 4) shows two separate gas temperature values: a warm ~ 120 K and a hotter ~ 200 K temperature. We used a range of temperatures (110–250 K) to derive a plausible mass for this component. Also, we refrain from deriving the mass and density of the disk, since it is optically thick and its dust millimeter emission may comprise an unknown contribution due to scattering. Añez-López et al. (2020) estimated the disk mass to be around $5 M_{\odot}$.

3.2. The GGD 27-MM1 Disk and Envelope System: Molecular Content

Figures 2 and 3 show a comprehensive view of some of the more common molecular species detected toward the disk of GGD 27-MM1 in the present Band 7 ALMA observations. They present velocity total integrated emission images (i.e., moment zero images) providing a glimpse of the spatial distribution diversity of the molecular emission. Complete velocity cube images, with the details on the gas kinematics, can be found in Appendix B.

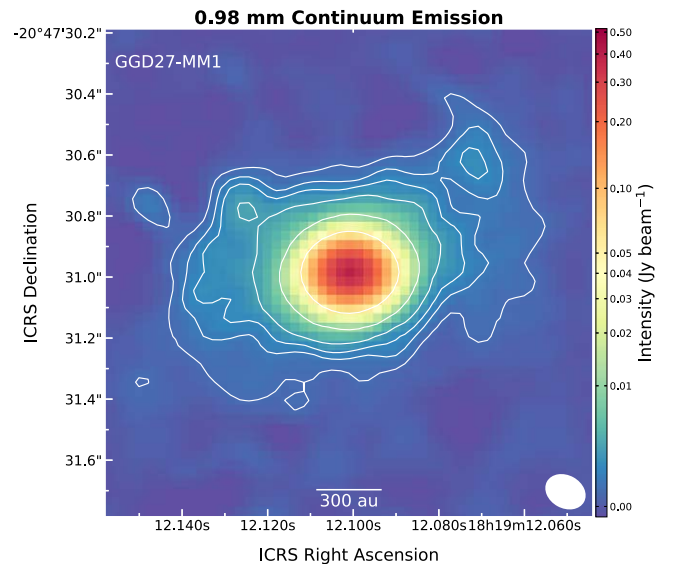


Figure 1. ALMA 0.98 mm dust continuum emission toward GGD 27-MM1. Contours display the emission at levels 5, 10, 15, 25, 75, and 375 times the rms noise level of the image, $\sim 0.14 \text{ mJy beam}^{-1}$. The synthesized beam is shown in the bottom right.

Panel (a) in Figure 2 shows the H₂S(3_{3,0}-3_{2,1}) line emission, which preferentially traces the molecular component of the disk structure (average radius of about 0".18, i.e., 250 au). This molecular component embraces the more compact dust continuum emission from the disk. A remarkable feature of the molecular disk¹⁰ is the weak intensity of its southern rim, while revealing

¹⁰ From now on we use the terms dust disk and molecular disk to designate the dust component of the disk (traced by the continuum emission carefully analyzed and modeled in Añez-López et al. 2020) and the molecular component of the disk (traced by several emission lines, and already reported by, e.g., Fernández-López et al. 2011b; Girart et al. 2018).

Table 2
MM1 Continuum Emission

Component	Position		Peak Intensity (mJy beam ⁻¹)	Flux Density (mJy)	Deconvolved Size (mas × mas, deg)
	R.A. (s) [18 ^h 19 ^m]	Decl. (arcsec) [-20° 47']			
Compact	12.101 ^a	30.95 ^a	23.0 ^b	23.0 ^b	Unresolved ^c
Disk	12.10079 ± 0.000004	30.98585 ± 0.00004	353.6 ± 0.3	656.6 ± 0.7	133.2 ± 0.3 × 89.6 ± 0.3, 113.1 ± 0.3
Envelope	12.1020 ± 0.0003	30.966 ± 0.003	9.6 ± 0.2	127 ± 2	564 ± 10 × 341 ± 7, 108 ± 2
NE	12.1258 ± 0.0003	30.765 ± 0.003	3.5 ± 0.2	3.5 ± 0.2	Unresolved ^c
NW	12.071 ^a	30.62 ^a	1.8 ± 0.2	6.0 ± 0.8	261 ± 2 × 124 ± 4, 29 ± 9

Notes. The positional uncertainties quoted are just statistical. The absolute astrometric error of the observations is 0^{''}.013.

^a Peak position fixed.

^b Flux fixed. The value has been scaled from 263 GHz (Girart et al. 2018; Añez-López et al. 2020), assuming a spectral index of 1.2.

^c Assumed to be unresolved.

a bright northwest crescent shape and southeast bright spot. These asymmetries are not present in the continuum emission, though. The H₂S line is also characterized by a strong absorption toward the inner part of the disk. Interestingly, the absorption peaks at different velocities (see Section 4.4 for more details). The H₂S velocity cube (Figure 16 in Appendix B) makes a nice example of a rotating annular disk, spreading from +5.0 to 19.5 km s⁻¹ in LSR velocity. In Section 4.2, we analyze the possibility that the asymmetries in the molecular disk and the inner absorption originated in a system comprising a hot flat continuum disk, immersed in a flared molecular disk structure, which contains colder gas inside.

HC₃N(33-32) emission (Figure 2, panel (b)) comprises three peaks northward of the inner part of the dust disk. Two of these peaks are prominent protuberances northwest (0^{''}.54 = 760 au, from the protostar location) and northeast (0^{''}.39 = 550 au from the protostar) of the dust disk. These protuberances spatially coincide with the NE and NW dust components identified in Section 3.1. The emission from the rotating molecular disk is very weak for this line (mainly seen at high velocities, Figure 17 in Appendix B) suggesting a different origin for most of this line emission. Besides, the emission from the three main locations does not match the pattern of rotation of the disk, when compared with the emission from H₂S (Figure 2, panel (a)). They appear mostly at the systemic and more redshifted velocities (>12.1 km s⁻¹). We note as well that, interestingly, the central absorption peaks at different radial velocities (see Section 4.4).

The H₂CO(4_{1,3}-3_{1,2}) line (Figure 2, panel (c)) shows more extended emission than the rest of the lines detected here spreading further beyond the boundaries of the extended dust envelope emission. Its moment zero has a prominent absorption hole at the center of the disk, surrounded by emission overlapping the continuum emission from the envelope. It shows the northwest and northeast protuberances aforementioned, plus two weak curved arcs starting at the western side of the disk with tails extending to the southeast.

In panel (d) of Figure 2, the CH₃OH(3_{1,2}-2_{0,2}) emission shows a prominent peak of emission east of the protostellar position. Contrarily to the disk rotation pattern (east/west are blueshifted/redshifted, respectively), this peak is contributed mainly by redshifted emission (velocities larger than 12.1 km s⁻¹, Figure 19 in Appendix B). There is also a 1^{''}.2 (850 au) curved arc starting from the western side of the disk with a tail pointing south. A second, much fainter 0^{''}.7 (950 au) arc-like structure, is seen south of the disk. This is more clearly seen in the velocity cube (Figure 21 in Appendix B). The width

Table 3
Dust Masses

Component	R_d (au)	T_d (K)	Mass (M_\odot)	N_{H_2} (10 ²² cm ⁻²)
Disk	190	300–600	≈5 ^a	... ^a
Envelope	790	110–150	0.19–0.26	8.9–12.4
NE	≲170	110–250 ^b	0.003–0.007	2.9–6.7
NW	250	110–150	0.008–0.012	3.7–5.2

Notes.

^a Value derived from fits to CH₃CN spectra (see Section 4.1 and Figure 5).

^b Values estimated from the fitting of the continuum emission using an α -viscosity disk model (Añez-López et al. 2020).

of these arcs is marginally resolved with deconvolved sizes ranging between ~0^{''}.12 and ~0^{''}.17 (i.e., about 200 au). In addition, the CH₃OH emission traces the northwest protuberance seen in the other lines.

The two bottom panels (e) and (f) of Figure 2 show the SO₂ integrated emission of two lines with different excitation temperatures. The emission from SO₂(12_{6,6}-13_{5,9}) is clearly more compact than that from SO₂(9_{2,8}-8_{1,7}). The former line ($E_{\text{up}} = 160$ K, panel (e)) traces the molecular disk, which is more extended than the compact dust disk. It also peaks northwest and northeast from the disk at the locations of the aforementioned NE and NW dust components. The main emission in this line delineates an annular-like structure, broken up at the southern rim (similarly to the H₂S emission), tracing the molecular disk. The SO₂(9_{2,8}-8_{1,7}) line ($E_{\text{up}} = 51$ K, panel (f)) shows the broken annular-shaped molecular disk structure as well, but it has more extended emission spreading over a wider region. A curved arc-like structure runs from the western side of the disk with a tail pointing southeast; a gaseous loop can be noticed northward as well. The central absorption is deeper in the SO₂(9_{2,8}-8_{1,7}) line than in the higher-excitation line SO₂(12_{6,6}-13_{5,9}).

In Figure 3 we show the moment zero image of the CH₃CN $J = 17_3 - 16_3$ line. We have detected several transitions of the CH₃CN $J = 17-16$ ladder (Table 1); we use this molecule in Section 4.1 to estimate the physical conditions of the disk and envelope toward GGD 27-MM1. The spatial distribution of the emission from this molecule is similar to that of the H₂CO (Figure 2, panel (c)). It is associated with the molecular disk, the absorption hole at its center, its immediate envelope material, the northern protuberances, and one of the curved arcs extending south from the disk's western side (like the one seen in the CH₃OH emission).

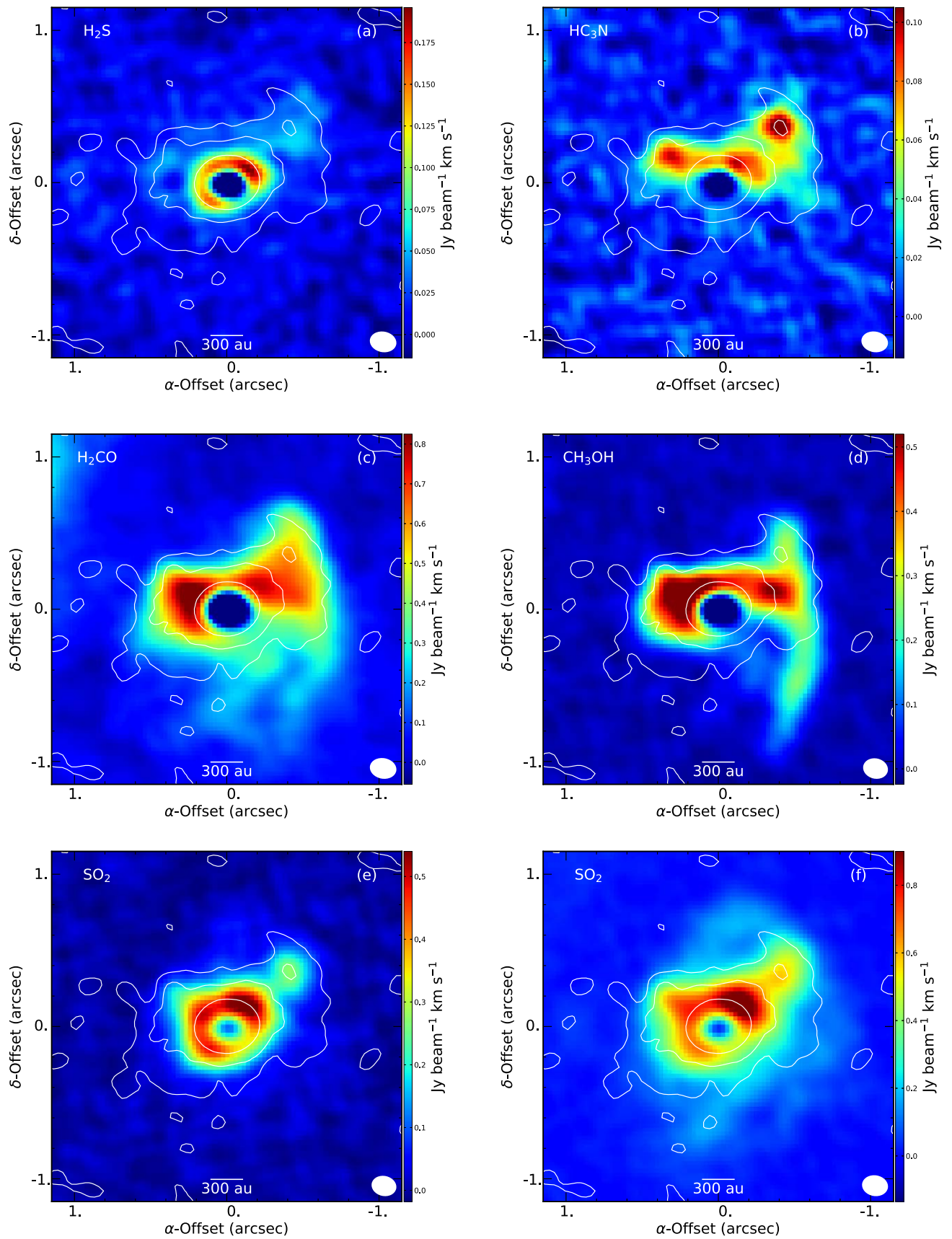


Figure 2. Following rows from top to bottom and panels from left to right, this figure presents the $\text{H}_2\text{S}(3_{3,0}-3_{2,1})$, $\text{HC}_3\text{N}(33-32)$, $\text{H}_2\text{CO}(4_{1,3}-3_{1,2})$, $\text{CH}_3\text{OH}(3_{1,2}-2_{0,2})$, $\text{SO}_2(12_{6,6}-13_{5,9})$, and $\text{SO}_2(9_{2,8}-8_{1,7})$ moment 0 images. Contours represent the continuum emission at 3, 15, and 100 times the rms noise level of $140 \mu\text{Jy beam}^{-1}$. Synthesized beams appear in the bottom right corner.

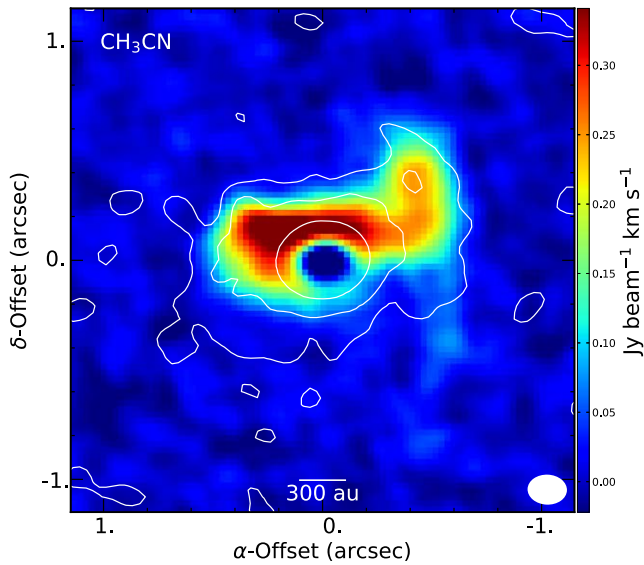


Figure 3. $\text{CH}_3\text{CN } J = 17_3-16_3$ moment 0 image with contours presenting the continuum emission as in Figure 2. The synthesized beam appears in the bottom right corner. The $K = 3$ is the strongest of the K -ladder transitions observed.

In a nutshell, we detect emission from a molecular diversity in GGD 27-MM1 (sulfured, carbonaceous, and oxygenated species). We identify some characteristic features closely related to the compact continuum dust disk (central absorption, molecular disk annular structure), and the extended envelope, which comprises the northern protuberances (NE and NW dust components) and the curved arcs. We find that different molecules preferentially exist in different regions. For instance, the sulfur-bearing H_2S appears related mostly to the molecular disk, but the also sulfurated SO_2 low-excitation lines trace the extended envelope and curved arcs as well. Likewise, the oxygenated CH_3OH shares some similitude (e.g., northern protuberances and curved arc) with the carbonaceous CH_3CN . Finally, the HC_3N and CH_3OH lines are weak in the molecular disk, contrarily to the rest of the chemical species; these lines preferentially trace gas structures in the vicinity of the molecular disk and also coincident with the NW and NE components, with velocities that do not belong to the rotation pattern of the molecular disk. The two southern curved arcs spatially coincide in CH_3OH and CH_3CN . The most prominent has a subtle difference in its curvature when seen in H_2CO . However, the low-excitation transitions of SO_2 trace preferentially emission from the easternmost arc with a slightly different trajectory.

4. Analysis

4.1. T_{ex} and Column Density from the CH_3CN Analysis

This section presents the analysis of the $\text{CH}_3\text{CN}(17-16)$ ladder detected with ALMA toward the GGD 27-MM1 disk. We derived excitation temperatures, column densities, and radial velocities of the gas using a manual, pixel-by-pixel spectral fitting using CASSIS¹¹ (see Appendix C for details on the fitting procedure and fitting examples in Figure 22). Before starting the fitting process, we spatially binned the ALMA data to build an image in which the pixels have the approximate size of the synthesized beam ($0''.17 \times 0''.13$). This allowed us to

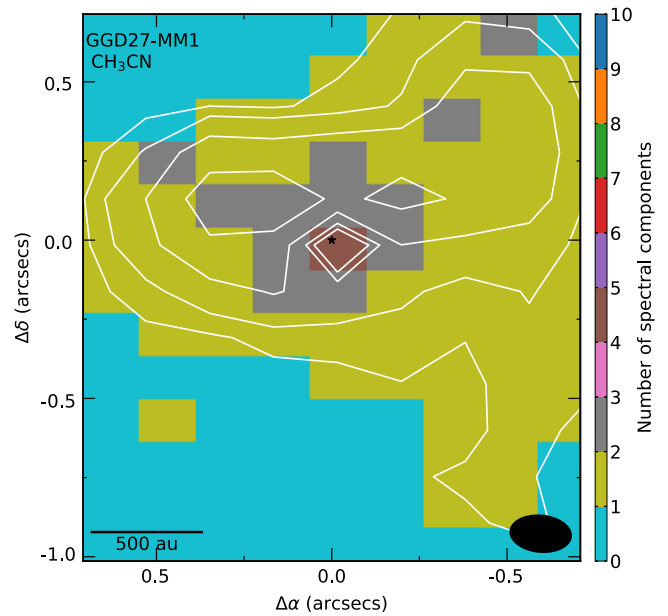


Figure 4. Number of velocity components found in the spectra of the $\text{CH}_3\text{CN } (17-16)$ ladder emission toward GGD 27-MM1. Contours show the integrated intensity from $\text{CH}_3\text{CN } K = 3$. Pixel size roughly coincides with the beam size.

analyze truly spatially independent spectra. Second, we identified the number of different spectral components in the spectrum of every pixel (Figure 4). The complex spectrum from the central pixel (coincident with the position of the continuum peak) contains at least four different spectral components. Surrounding this position, there is an annular-like set of pixels with two spectral components. There are two filament-like structures starting from this annulus and going northeast and northwest of the central position showing two spectral components, as well. The rest of the CH_3CN emission shows more simple spectra, presenting a single component.

After simultaneously fitting every spectral component at each pixel we could distinguish two different temperature-velocity-spatial structures toward GGD 27-MM1: (i) a hot and compact rotating structure, which we identify with the molecular disk, and (ii) a warm, extended, and more quiescent structure, which we identify with the molecular envelope. From this, we built two maps for the derived excitation temperature, CH_3CN column density, and radial velocity, separating the fitted solutions using a threshold of $T_{\text{ex}} = 200$ K, which clearly separates both structures (Figure 5).

An attempt to fit the CH_3CN absorption spectrum of the central pixel using a model with three components shows a good agreement with the observations. The fit and its results are shown in Section 4.4 (see also Figure 22 in Appendix C).

The top row of Figure 5 shows the results for the hot compact molecular disk, which has $T_{\text{ex}} > 200$ K, $N_{\text{CH}_3\text{CN}} \sim 2-4 \times 10^{15} \text{ cm}^{-2}$, and a clear velocity gradient along the disk major axis compatible with rotation (east is redshifted, west is blueshifted). In addition to the disk, the figure reveals two filament-like structures at velocities redshifted from the V_{LSR} velocity. The northeast filament particularly disagrees with the rotation pattern of the molecular disk, suggesting that these structures do not belong to the disk or envelope (which is colder), although may be physically connected. It is thereby plausible that they are part of two independent streamer-like structures.

¹¹ Analysis carried out with the CASSIS software (<http://cassis.irap.omp.eu>; Vastel et al. 2015) and the JPL and VAMDC databases. CASSIS has been developed by IRAP-UPS/CNRS.

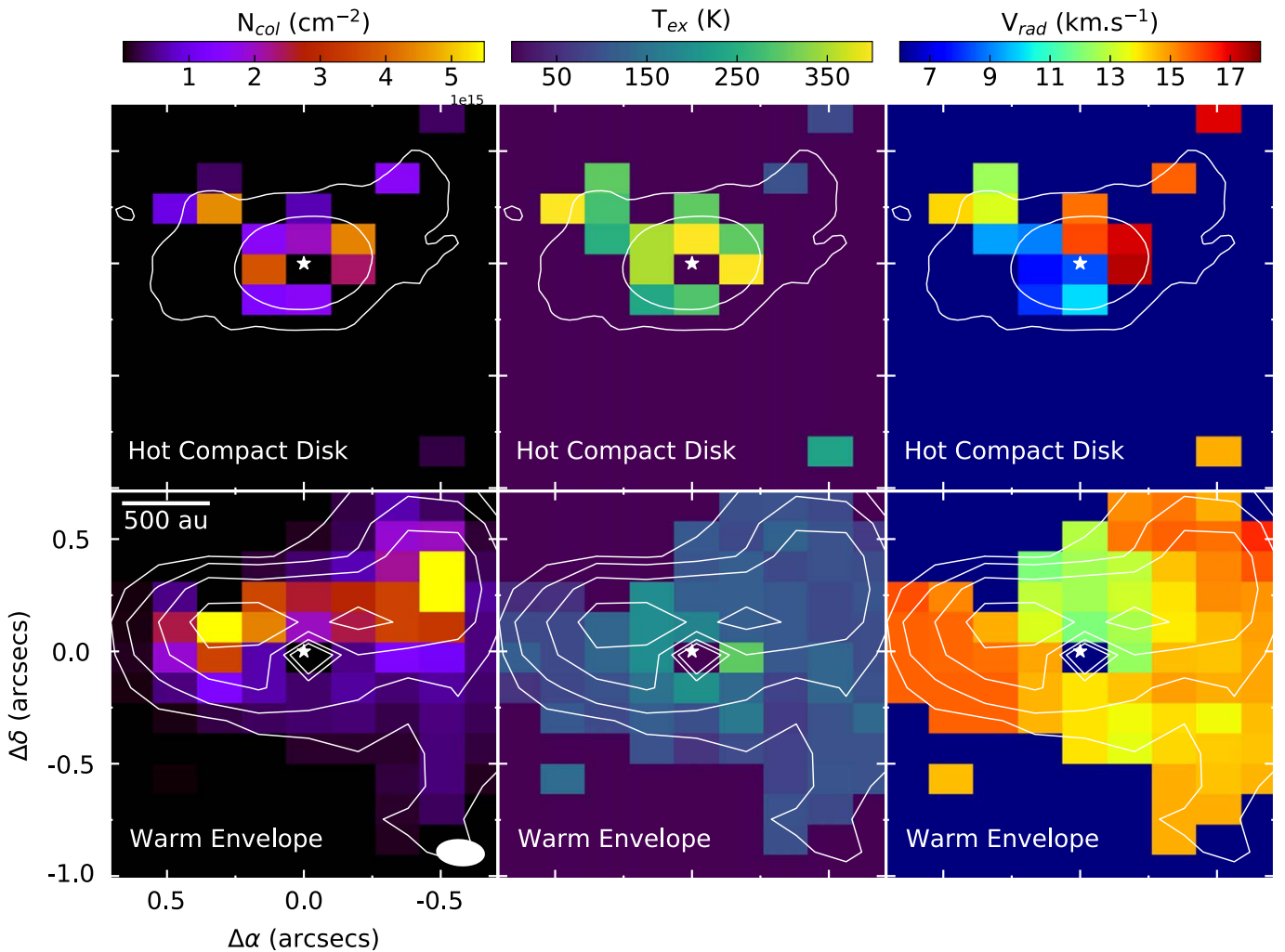


Figure 5. CH_3CN maps obtained from the fit to the compact hot molecular disk (upper panels), and the warm envelope (bottom panels). From left to right are the column density, $N_{\text{CH}_3\text{CN}}$, in units per square centimeter, the excitation temperature, T_{ex} , in units of K, and the LSR velocity, V_{rad} , in units of kilometers per second.

The bottom row of Figure 5 shows the gas from the warm envelope, which has $100 \text{ K} < T_{\text{ex}} < 200 \text{ K}$, $N_{\text{CH}_3\text{CN}} \sim 0.5\text{--}5 \times 10^{15} \text{ cm}^{-2}$, and velocities $13\text{--}15 \text{ km s}^{-1}$ close to the systemic, redshifted from the 12.1 km s^{-1} center of the rotating pattern of the disk, and not showing clear velocity gradients. The envelope shows a denser rim at the northern part of the disk, with two prominent peaks at both the east and west sides. These peaks are slightly redshifted from the rest of the envelope’s gas, which is also a bit more blueshifted north of the continuum peak. The temperature seems more uniform, slightly increasing toward the disk center.

Figure 6 presents annular averages of the excitation temperature, the column density, and the LSR line-of-sight velocity of the CH_3CN . The averages were calculated assuming a disk model with a position angle of 113° and an inclination of 49° (Girart et al. 2018; Añez-López et al. 2020). Black/red symbols denote the spectra from the hot disk/warm envelope components. The plots are divided into three zones (yellow, olive, and blue) separated at 330 and 790 au, corresponding with the centrifugal radius¹² that we estimate from the H_2S emission, following the procedure

¹² We follow the same procedure as Sakai et al. (2014) identifying the highest and lowest velocity peaks of the H_2S emission in a position–velocity diagram along the major axis of the disk. Their average position is $0''.12 \pm 0''.5$ ($166 \pm 70 \text{ au}$), which is the radius of the centrifugal barrier, likewise half of the centrifugal radius ($\sim 330 \text{ au}$).

described in Sakai et al. (2014), and the radius of the envelope (as measured in the continuum emission, see Table 3).

The CH_3CN excitation temperature (Figure 6, top panel) decreases with distance from the star up to 790 au. It shows a clear segregation between the hotter and warmer data points (i.e., between disk and envelope). To stress this segregation we set a temperature threshold at 200 K and use symbols with different colors for the hot and warm points (black and red, respectively). Several power laws (dotted lines) of the form $T \propto T_{100}(100/R)$ are plotted for values of T_{100} between 300 and 1500 K, where T_{100} is the excitation temperature at 100 au. The inverse linear trend is assumed following the derivation in Añez-López et al. (2020), who used a radiative code model to simulate the continuum emission of a flared disk of 170 au radius. If the gas is thermalized, the excitation temperature of the hot disk and warm envelope can be a proxy for dust temperature. The best model for the continuum disk emission resulted in a power law with $T_{100} = 300 \text{ K}$, but the molecular data do not have the spatial resolution to determine the temperature at 100 au. However, for radii $< 790 \text{ au}$ (i.e., the area within the envelope), the black dots show a $\sim 1/R$ trend with $T_{100} \gtrsim 750 \text{ K}$. Likewise, the red dots (warm envelope) apparently show a similar trend with a $T_{100} \gtrsim 300 \text{ K}$. This indicates that the gas temperature would be clearly higher than the dust temperature. Beyond the envelope’s outer boundary,

the temperature of the warm component (red dots) stays at ~ 100 K, while the hot component (black dots) reveals the presence of two hot spots.

The middle panel of Figure 6 shows the CH_3CN column density. There is no clear segregation between the disk and envelope data points. For distances < 790 au, the densities lie in a plateau, mostly between 3×10^{14} and $8 \times 10^{15} \text{ cm}^{-2}$; beyond that radius, densities are lower, ranging between 10^{14} and 10^{15} cm^{-2} . A clear trend of decreasing density with distance from the protostar is hampered due to some outliers; we overlapped the result trends derived in the continuum disk modeling by Añez-López et al. (2020) as guidelines for comparison. We used different values for the CH_3CN abundance, which seems to be between 10^{-10} and 10^{-11} (see Section 5).

The bottom panel of Figure 6 displays the CH_3CN radial profile of the V_{LSR} velocity. As expected the hot disk (black dots) shows a rotation pattern consistent with the overlapped Keplerian curves for central masses 5, 15, and $25 M_{\odot}$. The scarcity of sampling toward the inner region (lack of angular resolution), the lack of high-velocity gas, and the uncertainties on the measurements (lack of spectral resolution), hamper a finer determination of the central mass. Besides a more detailed analysis of the disk rotation shown by the H_2S emission resulted in no improvement in the accuracy of the mass determination, compared with the value obtained by Añez-López et al. (2020). The warm envelope (red dots) shows a different trend. It lies at low velocities (less than $\sim 4 \text{ km s}^{-1}$), is redshifted, and has a smooth increasing tendency further from the protostar. Close to the protostar there is envelope emission at least at two different velocities: one close to 0 km s^{-1} and another at about 2 km s^{-1} with respect to the systemic velocity of the rotating disk.

4.2. Flared Disk Model

Motivated by the broken annular shape (or crescent) of the H_2S $3_{3,0}-3_{2,1}$ integrated emission image toward GGD 27-MM1 molecular disk, this section presents a toy model that can explain it. Alternative ways to create a broken annular-shaped structure with an asymmetric brightness distribution can be attributed to the formation of substructures within the disk. Indeed, lopsided disks and crescent shapes have been seen to be originated from vortices in the dust traps of low-mass transitional disks or clumps infalling into the disk (e.g., van der Marel et al. 2021; Demidova & Grinin 2022). These types of disk asymmetries have been detected preferentially in the dust continuum emission.

The simple, phenomenological, model has three different components:

1. A central dust disk with radius R_{dust} devoid of line emission, seen in absorption after subtracting the continuum emission.
2. A flared molecular disk illuminated by the central protostar. The flared disk extends from an inner radius R_{inn} to an outer radius R_{out} .
3. Cold gas that fills the volume between the upper and lower lids of the flared disk with a nonzero optical depth, which, in this model, is responsible for the absorption of the continuum emission of the dust disk. Note, however, that in Section 4.4 we find that the H_2S absorption is probably caused by the absorption of foreground layers rather than an internal cold gas, since it does not show the expected

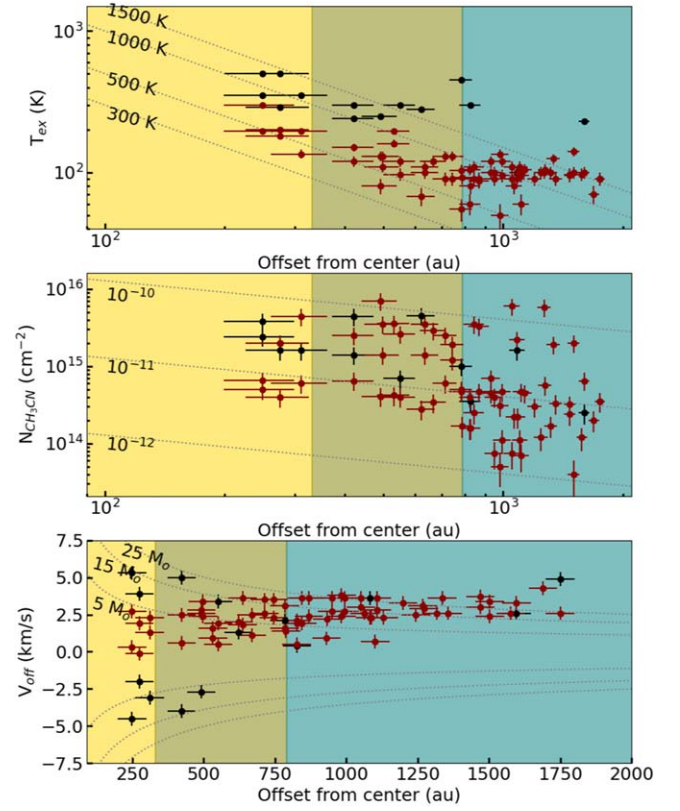


Figure 6. Radial behavior of the excitation temperature, column density, and offset radial velocity from the hot molecular disk component (black symbols) and the warm envelope component (red symbols). The spatial offsets are estimated assuming a disk/envelope model with a position angle of 113° and an inclination of 49° (0° for a face-on disk). The hot compact disk extends up to $R \simeq 360$ au. $T_{\text{ex}} \propto T_0/R$ (dotted curves for different values of T_0). $N_{\text{CH}_3\text{CN}} = (500 \cdot X_{\text{CH}_3\text{CN}} / (\mu_{\text{MH}})) \cdot \sqrt{100 \text{ au}/R}$ (dotted curves for various abundances $X_{\text{CH}_3\text{CN}}$). V_{off} velocity relative to the systemic velocity (12.1 km s^{-1}) vs. deprojected spatial offsets (the system inclination is taken into account). The dotted lines show the Keplerian rotation curves for different central masses. Offset error bars are 50 au, $\sim 1/4$ of the beam size.

(Keplerian) rotation pattern. Nevertheless, here we chose this cold gas filling the disk lids for our toy model.

The model has several geometrical and physical parameters that are described in detail in Appendix E. The disk is described by its center coordinates, the position angle, the inclination with respect to the line of sight, the radius, and the intensity of the dust emission. The intensity of the dust emission is taken as a power law of the radius, $I_{\text{rdust}} \propto r^{-1}$, (Añez-López et al. 2020). The dust disk is assumed to be optically thick and geometrically flat. The flared molecular disk comprises two lids with upper and lower conical faces (Figure 7). This disk is described by inner and outer radii, a flare angle, and the intensity of the two faces. The center, position angle, and inclination of the molecular disk are the same as those of the dust disk. Finally, we included cold gas filling the volume between the faces of the molecular disk. This gas is responsible for the absorption of the continuum emission of the disk and is parameterized through intensity and optical depth.

The results of the best fits of the phenomenological model to the integrated intensity H_2S data toward GGD 27-MM1 are presented in Table 4 and in Figure 8. Note that, for the fits, we did not consider the velocity structure of the emission and we just used the integrated intensity. The model that works best (i.e., minimizes the residuals) is one with an inner compact dust disk of 60 ± 14 au

radius. This size is smaller than the one that results from the radiative transfer modeling of the continuum emission and the size of the continuum emission. This may indicate that only the central part of the disk (the hottest part) is being absorbed by the cold gas and that there is a strong drop in the dust temperature within 100 au from the central protostar. The molecular disk extends from 140 to 360 au in radius (which agrees well with measurements from the moment 0 image along the major axis) and has a flare angle (measured from the midplane to one of the conical lids) of $11 \pm 4^\circ$. The gas between the lids of the disk is cold and optically thick, while the warm faces of the gas disk would be heated by the protostellar radiation. The dust emission from the disk corresponds to a brightness temperature, about 4 times that of the gas disk lids, and more than 30 times larger than that of the cold gas.

The flared disk model fits qualitatively the central absorption, the dim of the southern part of the H_2S emission, and the crescent-like features of its northern part, leaving residuals between 2 and 3 times the noise level. It allows us to obtain the flare angle and the width of the molecular disk.

4.3. Possible Accretion Streamers

In Section 3.2 we showed that the spatial distribution of the emission of various molecules (H_2CO , CH_3OH , SO_2 , CH_3CN) have elongated and curved structures, connecting the outer envelope with the envelope/disk system. A plausible explanation is that these structures form a complex system of streamers that drive material from the outer parts of the original cloud surrounding GGD 27-MM1 onto the inner envelope, or even toward the equatorial plane of the disk. These streamers could even transform into rotating spiral arm-like structures when reaching the envelope. The streamers can comprise gas from the original cloud that may have been dragged and pushed by the thermal jet, and is now infalling onto the disk. Alternatively, the structures could be the shreds of gas associated with a fly-by passage through the disk of widely separated companions, or the tidal streams from a close encounter (Cuello et al. 2023). However, these latter scenarios have no current observational support (i.e., no companions have been confirmed so far associated with GGD 27-MM1). Motivated by the recent discovery of accretion streamers in other circumstellar disks (e.g., Yen et al. 2014, 2019; Alves et al. 2020; Pineda et al. 2020; Hsieh et al. 2020; Huang et al. 2021; Thieme et al. 2022), we analyze this hypothesis by fitting a model to the gas emission of the streamers more clearly identified.

We assumed that the material of the observed gas streamers comes from the original accreting envelope. If the material of the envelope has a certain amount of angular momentum and zero total energy, it should follow a parabolic trajectory in which the focus corresponds to the origin of the coordinates system (Ulrich 1976, hereafter Ulrich’s model). These trajectories projected onto the plane of the sky can form similar structures to the observed streamers (Yen et al. 2014).

Ulrich’s model considers that the accreting envelope is a rotating cloud in gravitational collapse, where the fluid particles, initially at rest, have a distribution given by a rigid body rotation, falling to the center and conserving the specific angular momentum. The collapse is assumed to be pressureless and thus the orbits are ballistic. When the fluid particles approach the equatorial plane, they collide with their symmetric counterparts, where they could form an equatorial disk around the central object.

More recently, Mendoza et al. (2009) (hereafter Mendoza’s model) proposed an analytic accretion envelope where the

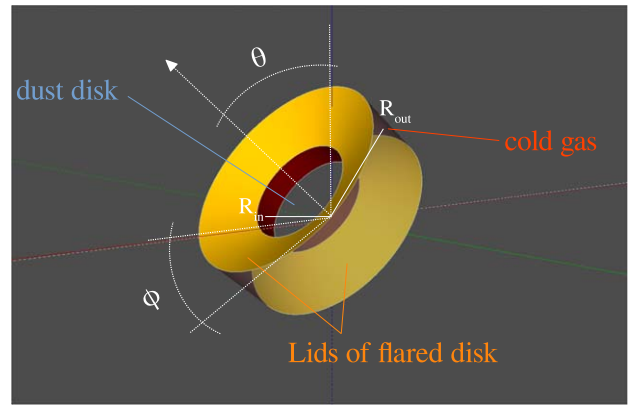


Figure 7. Flared disk model for the H_2S emission comprising three components: a compact dust disk (indicated but not shown in the sketch), a conical truncated flared molecular disk, whose lids are seen in emission, and an optically thick cold gas filling the volume between the conical lids.

Table 4
Best-fit Results from the Flared Disk Model

Param.	Units	Value	Description
x_0	(mas)	3.2 ± 3.7	Center coordinate
y_0	(mas)	-0.4 ± 3.8	Center coordinate
θ	(deg)	112.9	Disk-axis position angle (fixed)
i	(deg)	40.8	Inclination (fixed; 0 if face-on)
ϕ	(deg)	11.0 ± 3.6	Flare angle (from the midplane to lid)
R_{dust}	(au)	60 ± 14	Dust-disk radius
R_{in}	(au)	141 ± 17	Disk inner radius
R_{out}	(au)	357 ± 9	Disk outer radius
I_{dust}	(K km s $^{-1}$)	498 ± 80	Dust-disk intensity at 100 au
I_{face}	(K km s $^{-1}$)	125 ± 14	Flare-disk intensity
I_{cold}	(K km s $^{-1}$)	<16	Cold-gas intensity
τ_0	...	>18	Cold-gas opacity
Fit rms	(K km s $^{-1}$)	12.3	

radius of the rotating cloud or accreting envelope is finite and the fluid particles can have an initial radial velocity (i.e., not a line-of-sight velocity but a velocity component in the direction to the central protostar). Also, the orbits are contained in a plane and are described by conic sections. More specifically, the trajectories of the fluid particles are given by

$$r = \frac{\sin^2 \theta_0}{1 - e \cos \varphi}, \quad (1)$$

where r , θ , and ϕ are the spherical coordinates, and the radius r is expressed in units of the equatorial disk radius (from now on the inner radius, r_{in}) where the material streams to, θ_0 is the initial polar angle of the orbit of the fluid element at the beginning of the collapse toward the center, and φ is the azimuthal angle over the plane orbit. Finally, e is the eccentricity of the orbit given r by

$$e = \sqrt{1 + \varepsilon \sin^2 \theta_0}. \quad (2)$$

The variable ε is the dimensionless specific energy. Under the assumptions of Mendoza’s model, the energy is constant along each particular trajectory. This energy can be written as

$$\varepsilon = \nu^2 + \mu^2 \sin^2 \theta_0 - 2\mu, \quad (3)$$

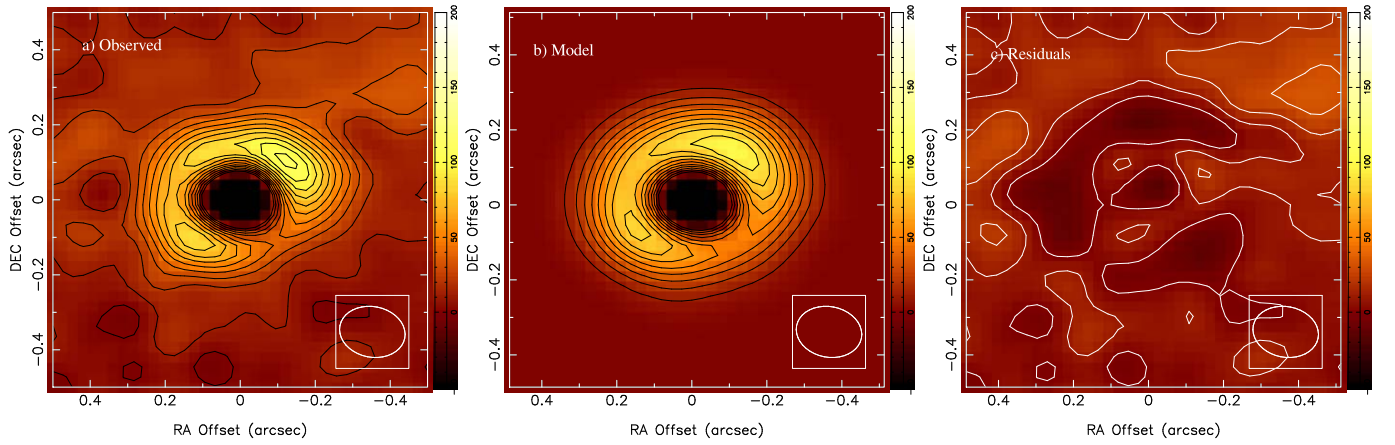


Figure 8. Flared disk model for the H_2S emission. From left to right, the images show the observed moment 0 integrated intensity image, the model obtained (see Appendix E), and the residual image after the fit. The three images have the same color scale and contours, at multiples of 10 K km s^{-1} . Their rms noise value is 5 K km s^{-1} . The beam is shown at the bottom right corner of each image.

where the parameter ν is the ratio between the initial radial velocity and the Keplerian velocity, and the parameter μ is the ratio between the inner radius r_{in} and the radius of the rotating cloud or accreting envelope r_0 ($\mu = r_{\text{in}}/r_0$). At the border of the cloud, $r = r_0 = 1/\mu$. If we use this condition in Equation (1), we obtain the following condition for φ_0 :

$$\cos \varphi_0 = \frac{1}{e}(1 - \mu \sin^2 \theta_0). \quad (4)$$

We can define this angle as the initial position of the particle trajectory in the orbital plane.

The trajectory of the fluid particles is defined by the angles φ , θ , θ_0 , ϕ , and ϕ_0 , where θ and ϕ are the polar and azimuthal coordinates, respectively. The variables θ_0 and ϕ_0 are the polar and azimuthal initial angles, respectively. These angles are related between them as

$$\cos(\varphi - \varphi_0) = \frac{\cos \theta}{\cos \theta_0}, \quad \cos(\phi - \phi_0) = \frac{\tan \theta_0}{\tan \theta}. \quad (5)$$

In terms of the angles defined in the above equation, the radius and velocity field of the accretion envelope in Mendoza's model can be written as

$$r = \frac{\sin^2 \theta_0}{1 - e \cos \xi}, \quad (6)$$

$$v_r = -\frac{e \sin \xi \sin \theta_0}{r(1 - e \cos \xi)}, \quad (7)$$

$$v_\theta = \frac{\sin \theta_0}{r \sin \theta} (\cos^2 \theta_0 - \cos^2 \theta)^{1/2}, \quad (8)$$

and

$$v_\phi = \frac{\sin^2 \theta_0}{r \sin \theta}, \quad (9)$$

where the angle ξ is given by

$$\xi = \cos^{-1} \left(\frac{\cos \theta}{\cos \theta_0} \right) + \phi_0. \quad (10)$$

If we fix $\mu = 0$ and $\nu = 0$, the radius and velocity field of Mendoza's model converge to the solutions of Ulrich's model, a more detailed comparison between both models is presented in Appendix D.

For the purpose of testing the accretion streamer scenario in GGD 27-MM1, we identify some curved arcs analyzing the $\text{CH}_3\text{OH}(3_{1,2}-2_{0,2})$ emission. We named these structures S1, S2, and S3 (Figure 9). These structures can also be identified in the $\text{H}_2\text{CO}(4_{1,3}-3_{1,2})$ moment 0 image (Figure 2). For each of these structures, we selected gas condensations of the CH_3OH emission by carefully inspecting its channel maps (Figure 19 in Appendix B). We considered condensations with intensity peaks of at least 5σ . We additionally avoided the area close to the molecular disk, where emission from several structures is blended at the resolution of the present ALMA observations. S1 is related to the northwest protuberance which seems to connect with the northwest part of the disk (Figure 2 and channel maps from $14-17 \text{ km s}^{-1}$ in Figure 19 in Appendix B); S2 is a $\sim 1''$ curved arc with the tail pointing south and connecting with the west side of the disk (Figures 2 and 19); S3 corresponds with the second fainter arc with the tail pointing southeast that connects with the southwest part of the disk (Figure 2 and channel maps from $11.5-14.0 \text{ km s}^{-1}$ in Figure 19 in Appendix B). Despite the method of identifying the streamer's condensations can be refined with higher angular resolution observations, the idea of the analysis is just to check the plausibility of the accretion streamer scenario.

In order to explain the S1, S2, and S3 streamers we use both Ulrich's model and Mendoza's model. We adopted a stellar mass of $M_* = 20M_\odot$ (Añez-López et al. 2020), an inclination angle of the disk and the envelope system with respect to the plane of the sky of 42° (Table 4), and a position angle of 113° . Also, we consider two different inner radii r_{in} for the fits. First, the molecular disk outer radius of 357 au (see Table 4); second, the envelope radius of 790 au (see Table 2). The angles θ_0 and ϕ_0 are left as free parameters in both models. For Mendoza's model, μ and ν are left as free parameters too.

The best set of parameters fitting the data are shown in Table 5 for both models. These parameters were estimated using the so-called *asexual genetic algorithm* (AGA) developed by Cantó et al. (2009).

Figure 10 shows two panels with the CH_3OH integrated intensity emission (moment 0) in color scale. In these plots, the streamers denoted by S1, S2, and S3 (see Figure 9) can be observed. The white triangles, circles, and squares show the position of the CH_3OH condensations identified in the velocity cube on a channel-by-channel basis. The solid lines correspond to

our best fits manually found using parabolic orbits (Ulrich’s model), while the dashed lines represent the conic orbits (Mendoza’s model). The left panel shows the models for r_{in} equal to the molecular disk radius, while the right panel presents the models for r_{in} equal to the envelope radius. Both models fit reasonably well the observational data and could explain the trajectories of the streamers. However, Ulrich’s model cannot reproduce the curvature of the streamer S2. In addition, the curvature of the streamer S1 is contrary to S2 and S3. This could mean that S1 is rotating in the opposite direction. Alternatively, S1 could be associated with material that has already reached the periastron and has crossed the plane of the accretion disk.

The position–velocity diagrams along the streamers S1, S2, and S3, are shown in Figure 11. The solid and dashed lines represent our best fits using Ulrich’s model and Mendoza’s model, respectively (same as in Figure 10). The top panels present the models where r_{in} equals the molecular disk radius, and the bottom panels show the models where r_{in} equals the envelope radius. The triangles, circles, and squares correspond to S1, S2, and S3 condensations (same as in Figure 10). The panel in this figure shows that both models can roughly match the velocities in the streamers. Both models show a lack of detailed coincidence, which could be motivated by coarse angular and spectral resolutions and the manual selection of the putative streamer trajectories. The velocities obtained using the AGA algorithm should be considered as a rough approximation to the observational line-of-sight velocities, since the simple models used do not consider different physical phenomena such as the thermal pressure, the magnetic pressure, or the expansion of MM1’s outflow.

Figure 12 presents the line-of-sight velocity for our best-fit trajectories found using Mendoza’s model in the three streamers. We chose to use Mendoza’s model because Ulrich’s model cannot fit the curved trajectories of the streamers. In this figure, we made a comparison between the line-of-sight velocities obtained from Mendoza’s model and those measured in the CH₃OH condensations. The left panel corresponds to the model where r_{in} is the molecular disk radius and the right panel represents the model where r_{in} is the envelope radius. A few contours of the continuum emission are shown for reference purposes.

4.4. Molecular Absorption in the Inner Region of the Disk

Figure 13 shows the absorption feature in the spectra toward the center of the disk ($0''.2 \times 0''.2$ box, or 280×280 au at the source distance) in the H₂S $3_{3,0}-3_{2,1}$ transition (Table 1). This figure presents one spectrum of approximately every quarter of the synthesized beam. The emission in these spectra nicely shows the well-known rotation pattern of the disk—a southeast (blueshifted) northwest (redshifted) gradient—but the most noticeable feature is the broad absorption toward most of the positions (between 10.5 and 16.5 km s⁻¹). The H₂S absorption peaks do not follow a pattern of rotation analogous to that of the emission; they do not trace a velocity gradient along the inner disk positions. This can indicate that the absorption is produced in colder and more quiescent foreground layers, not sharing the disk kinematics, or in the cold flared structure from the southern rim, roughly aligned with the disk’s minor axis, which may not display significant rotation features. The absorption features mainly peak at redshifted velocities and they are more prominent southward of the continuum peak, marked with a star symbol. Moreover, there seem to be three main absorption peaks at velocities 13.0, 14.5, and 16.0 km s⁻¹.

We integrated the spectra of several molecular transitions found in the ALMA observations over the central beam of the GGD 27-MM1 disk (Figure 14). Some of these lines trace mainly the gas of the hot molecular disk (e.g., H₂S, SO₂), some others trace the colder envelope as well (e.g., CH₃CN ladder, H₂CO, SO₂). As can be seen in the three panels of Figure 14 (one for the CH₃CN ladder, one for the SO₂ lines, and one for the other absorbed transitions), most of the lines show redshifted absorption in the same velocity range as H₂S. However, different species show a different number of absorption peaks. While the H₂S line shows three peaks, the CH₃CN, CH₃OH, and H₂CO lines show two peaks at 13.0 and 16.0 km s⁻¹, and the SO₂ lines show one absorption peak at ~ 12.5 km s⁻¹.

Figure 14 (middle panel) shows that the two SO₂ lines with absorption have upper-energy levels (E_{up}) lower than 200 K. The only line that does not follow this trend is SO₂[12_{6,6}-13_{5,9}].

For the CH₃CN lines of the $J = 17-16$ K ladder, the ALMA data show absorption profiles with two peaks at 13.5 and 16.5 km s⁻¹. The absorption at 13.5 km s⁻¹ is noticeable from line $K = 0$ to $K = 7$ ($E_u = 250$ and 485 K, respectively). The $K = 5$ line is contaminated by other molecular transitions and does not show a clear profile. Interestingly, the absorption at 16.5 km s⁻¹ is only significant up to $K = 4$. The emission of the ladder is detected up to the $K = 9$ line (with $E_u = 713$ K). The differences in the spectra from these two absorption peaks could indicate the presence of two different kinematic components, with different physical properties.

Finally, at the central pixel, the fit of the CH₃CN K ladder is more complicated than for the rest. The line profile shows two redshifted absorption peaks and two emission peaks: one blueshifted and the other redshifted. Given the degeneracy in the space of parameters resulting from using that many spectral components, we choose to fit the profile using a simple approach comprising three interacting layers in CASSIS: (i) a background emission layer with uniform temperature corresponding with the dust continuum emission from the compact disk, (ii) a layer corresponding to the gaseous component of the hot disk, and (iii) a foreground layer corresponding to the warm envelope. As a proof of concept, we fixed the background temperature to a uniform value close to that reported in Añez-López et al. (2020) (300 K at 100 au from the central star). However, fixing this parameter has an important effect on the excitation temperatures of the other two layers (the disk of gas and the envelope). Hence, we have repeated the fit using temperatures from 250–450 K in steps of 50 K. The fits are qualitatively similar and the fit residuals are minimum between 250 and 300 K. The results of the spectrum fit (Table 6, Figure 24 in Appendix C), qualitatively agree with the warm envelope and hot disk picture outlined in this work, but the simplicity of the model leaves large uncertainties that ask for more information at the center of the system. Higher angular and spectral resolution observations of photodissociated gas tracers may give further evidence for a more detailed characterization. Despite this, one relevant takeaway is that the full width at zero intensity of the emission line is smaller than 14.5 km s⁻¹ for any line reported here (i.e., they show emission at maximum from +5.0 to 19.5 km s⁻¹). This would imply probing the rotating molecular gas at a radius of 340 au from the central 20 M_{\odot} protostar (if the mass of the protostar is 10 M_{\odot} , the radius would be 170 au).

4.5. Accretion Rate

The redshifted absorption in the spectra of molecules tracing the envelope and/or disk material surrounding a protostellar

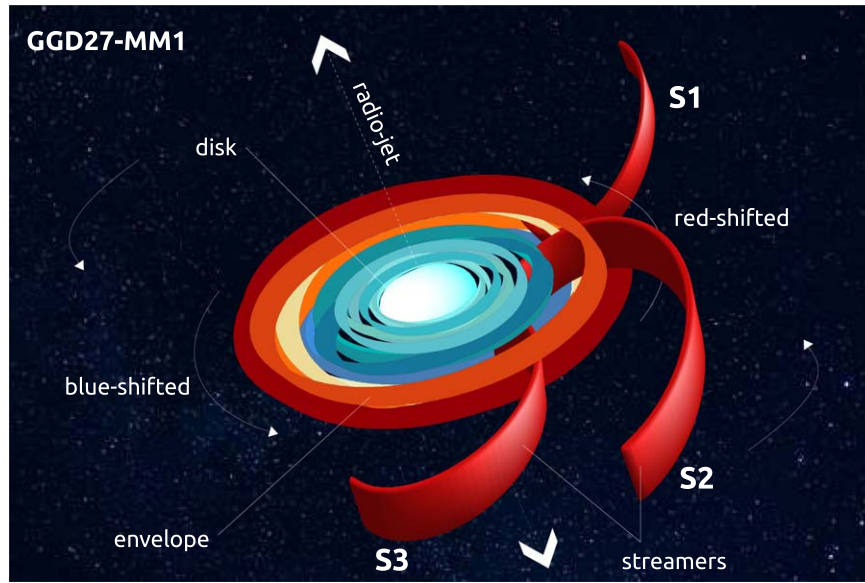


Figure 9. Sketch showing the disk, envelope, and the location of three possible accretion streamers: S1, S2, and S3. The figure indicates the approximate orientation of the thermal radio jet HH 80-81, of the disk and the system rotation. The rough representation is not to scale.

Table 5
Values of the Different Parameters Used for the Best Fits in the Two Models Considered and the Three Different Streamers

Radius (au)	Streamer	Ulrich's Model		Mendoza's Model			
		θ_0 (deg)	ϕ_0 (deg)	μ	ν	θ_0 (deg)	ϕ_0 (deg)
357	S1	52.55	108.68	0.35	0.13	121.19	94.804
	S2	73.59	283.16	0.56	0.97	144.30	325.64
	S3	128.32	251.44	7.9×10^{-2}	3.8×10^{-2}	116.02	256.09
790	S1	63.43	133.79	0.27	0.44	58.12	152.04
	S2	76.99	254.21	0.54	5.8×10^{-3}	72.21	289.60
	S3	117.84	226.65	0.46	3.1×10^{-2}	56.06	236.76

system can be interpreted as an inverse P Cygni line profile, originated by active accretion of material. In the case of GGD 27-MM1, the absorption is seen at the center of the system, within the inner 190 au, but the ALMA data also reveals two other signatures related to accretion processes: the redshifted quiescent material from the warm extended envelope and the accretion streamers (Sections 4.1 and 4.3). On one hand, we now assume that the redshifted absorption is due to gas moving inward toward the center. On the other hand, we assume that there is ongoing accretion from the extended envelope into the hot gaseous disk component. Following these hypotheses, we can apply an analogous procedure to that described in Beltrán et al. (2006) and Beltrán et al. (2022) to estimate the mass accretion rate at two highlighted radii: (i) the centrifugal radius, 330 au, which roughly coincides with the outer radius of the H₂S gas disk (~ 360 au) and (ii) the dust disk radius, of 190 au. These radii were picked to make estimates of the (i) infalling rate from the extended envelope onto the hot disk, and (ii) of the accretion rate from the external parts of the hot disk (mostly molecular) onto the dust disk. We use the expression

$$\dot{M}_{\text{acc}} = \Omega R^2 m_{\text{H}_2} n_{\text{H}_2} v_{\text{acc}}, \quad (11)$$

where $m_{\text{H}_2} = \mu \cdot m_{\text{H}}$ is the mass of the hydrogen molecule (we use $\mu = 2.8$ as the mean mass per H₂ molecule, see Kauffmann et al. 2008), R is the radius at which the rate is calculated, n_{H_2} is the H₂ column density at radius R , and v_{acc} is the infalling

accretion velocity. We approximate

$$n_{\text{H}_2}(R) = \frac{N(R)}{H(R)} = \frac{N(R_0)}{H(R_0)} \left(\frac{R}{R_0} \right)^{-1.5}, \quad (12)$$

where $H(R)$ is the height of the disk at radius R , which we assume is proportional to R . Likewise, the column density N goes as $R^{-0.5}$, as derived from the modeling by Añez-López et al. (2020). Using expressions (11) and (12), the mass accretion rate is

$$\dot{M}_{\text{acc}} = \Omega R^2 m_{\text{H}_2} \frac{N(R_0)}{H(R_0)} \left(\frac{R}{R_0} \right)^{-1.5} v_{\text{acc}}. \quad (13)$$

We derive the infall velocity measuring the velocity of the two main peaks in the CH₃CN line profiles of the $J = 17-16$ ladder (at 13.5 and 16.5 km s⁻¹, Figure 14); therefore, we estimate v_{acc} to be between 1.4 and 4.4 km s⁻¹ (2.0 and 6.2 km s⁻¹, corrected by projection, in case that the accretion is through the disk midplane). For the column density of the disk, we assume the relationship derived via radiative transfer modeling of the 1.14 mm continuum emission (see Equation (3) of, Añez-López et al. 2020). This results in $N = 7.8 \times 10^{25}$ cm⁻² at radius $R_0 = 190$ au. Extending the density trend up to 330 au gives a density of $N = 5.9 \times 10^{25}$ cm⁻². For an isotropic infall, the mass accretion rate will be in the range of 0.03–0.09 M_{\odot} yr⁻¹ at 190 au, which is

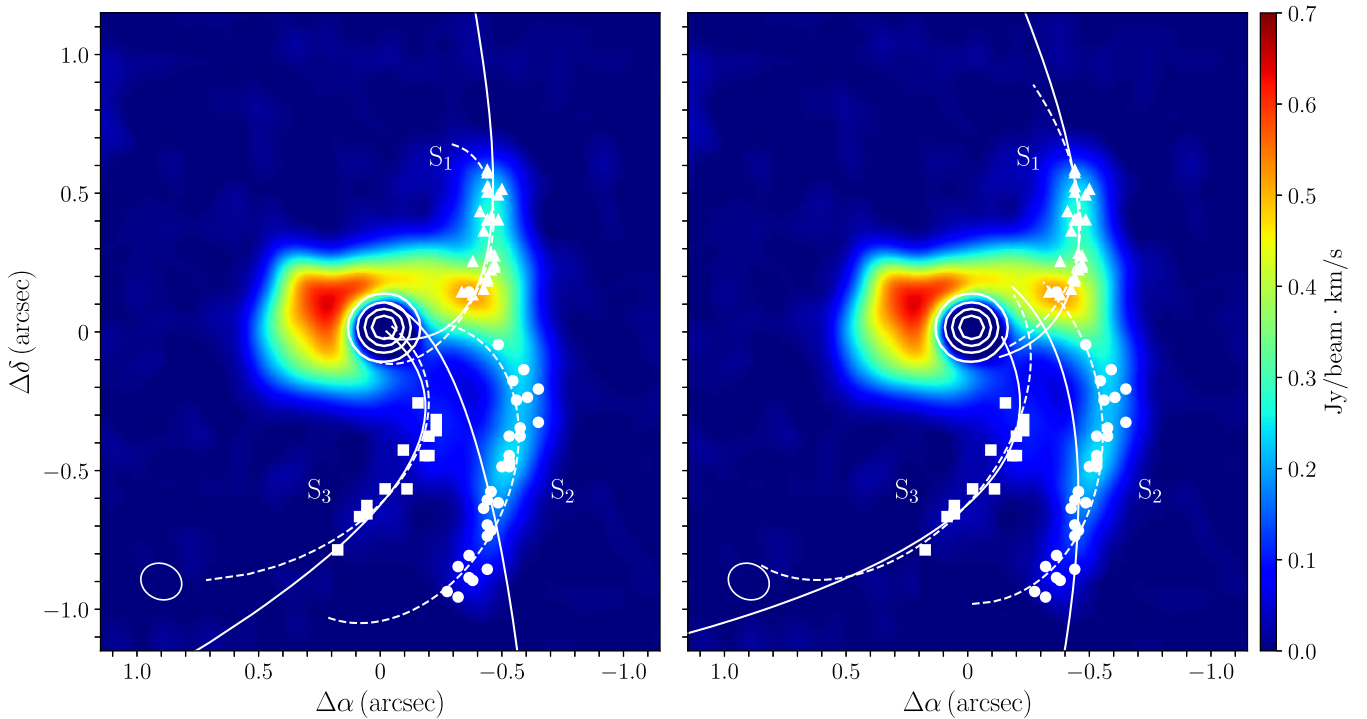


Figure 10. CH_3OH moment 0 image with contours representing the strongest continuum emission. In both panels, the solid lines represent Ulrich’s model while the dashed lines show Mendoza’s models (see the text in Section 4.3). Left panel: models using the inner equatorial radius, r_{in} , as the molecular disk radius (357 au). Right panel: same but using r_{in} as the envelope radius (790 au). The angles ϕ_0 and θ_0 and the parameters μ and ν of the fits are shown in Table 5. The triangles, circles, and squares mark the position of the condensations identified in the CH_3OH velocity cube.

3 orders of magnitude larger than the accretion onto the protostar estimated by Añez-López et al. (2020) ($7 \times 10^{-5} M_{\odot} \text{ yr}^{-1}$). However, we can consider that the bulk of the accretion process is not spherical but goes through a smaller solid angle, Ω . As a raw estimate of this factor, we take into account the vertical profile of the dust disk estimated in Añez-López et al. (2020). They estimated that the hydrostatic scale height of the disk would be 13 au at a radial distance of 190 au from the center. This implies a disk semi-opening angle of 4° . From the model of the H_2S disk emission the total flare angle of the disk would be 22° (see Section 4.2). This implies a mass accretion rate 1 order of magnitude smaller, ranging from $7 \times 10^{-4} - 1.24 \times 10^{-2} M_{\odot} \text{ yr}^{-1}$ at 190 au, and a larger $5.2 \times 10^{-3} - 1.64 \times 10^{-2} M_{\odot} \text{ yr}^{-1}$ at 330 au (for this latter distance from the protostar, we use only the large flare value of 22°).

5. Discussion

The ALMA data presented in this work reveals that the GGD 27-MM1 protostellar system comprises four different structures. (i) At small scales, surrounding the protostellar object(s), there is a dust continuum disk, with a radius estimated in 170–190 au; (ii) encompassing the dust there is a rotating hot gaseous disk, seen in emission between 140 and 360 au; (iii) a more spread envelope, roughly 1600 au in diameter, detected in dust emission but also in several molecular components; (iv) at least three molecular accretion streamers with lengths between 850 and 1700 au apparently bridging external material onto the disk structure.

5.1. The Compact Continuum Disk

Regarding the kinematics of the compact dust disk, the central emission/absorption detected in several species does not show the

larger velocity spread expected in the inner part of a rotating structure. For the H_2S line, the radial velocity ranges from $+5.0$ to $+19.5 \text{ km s}^{-1}$ in the LSR, suggesting a rotation velocity of $\sim 7.25 \text{ km s}^{-1}$ at the innermost radius of its emission. However, for a $20 M_{\odot}$ central star, the expected Keplerian velocity at, for example, 20 au, would be 30 km s^{-1} . If the central mass estimate is accurate enough, this implies that the molecular content detected in the GGD 27-MM1 disk reaches an innermost radius of ~ 340 au, which is approximately twice the 141 au of the inner radius derived from our phenomenological molecular model (see Section 4). To reconcile these two radii, the central mass should be about $10 M_{\odot}$, or the measured rotation motions are sub-Keplerian. The lack of molecular emission at high velocities could explain the problems constraining the dynamical mass of the system and, more generally, the problems probing the Keplerianity of high-mass protostellar disks and pseudo-disks. A possible explanation for the lack of molecular emission inward of this radius at large velocities is that there is not much molecular content left embedding the compact continuum disk may be due to photoevaporation and/or radiation pressure. The radiation pressure effect is less likely since it is various orders of magnitude lower in molecules than in dust grains. Therefore, the lack of abundant molecular material in the inner part of the system is more likely due to photodissociation and/or photoevaporation. Interestingly, while this inner region is apparently devoid of molecular gas at high velocities, the radiation has not destroyed the dust grains at the disk’s midplane yet. Actually, the dust is optically thick at the inner part and could hide the molecular remnants within the $\tau = 1$ layer, completely absorbing their emission. The emission/absorption detected at the central position seems to come from gas from the inner radius of the molecular disk component and from the continuum radiation absorbed by the tenuous and widespread envelope.

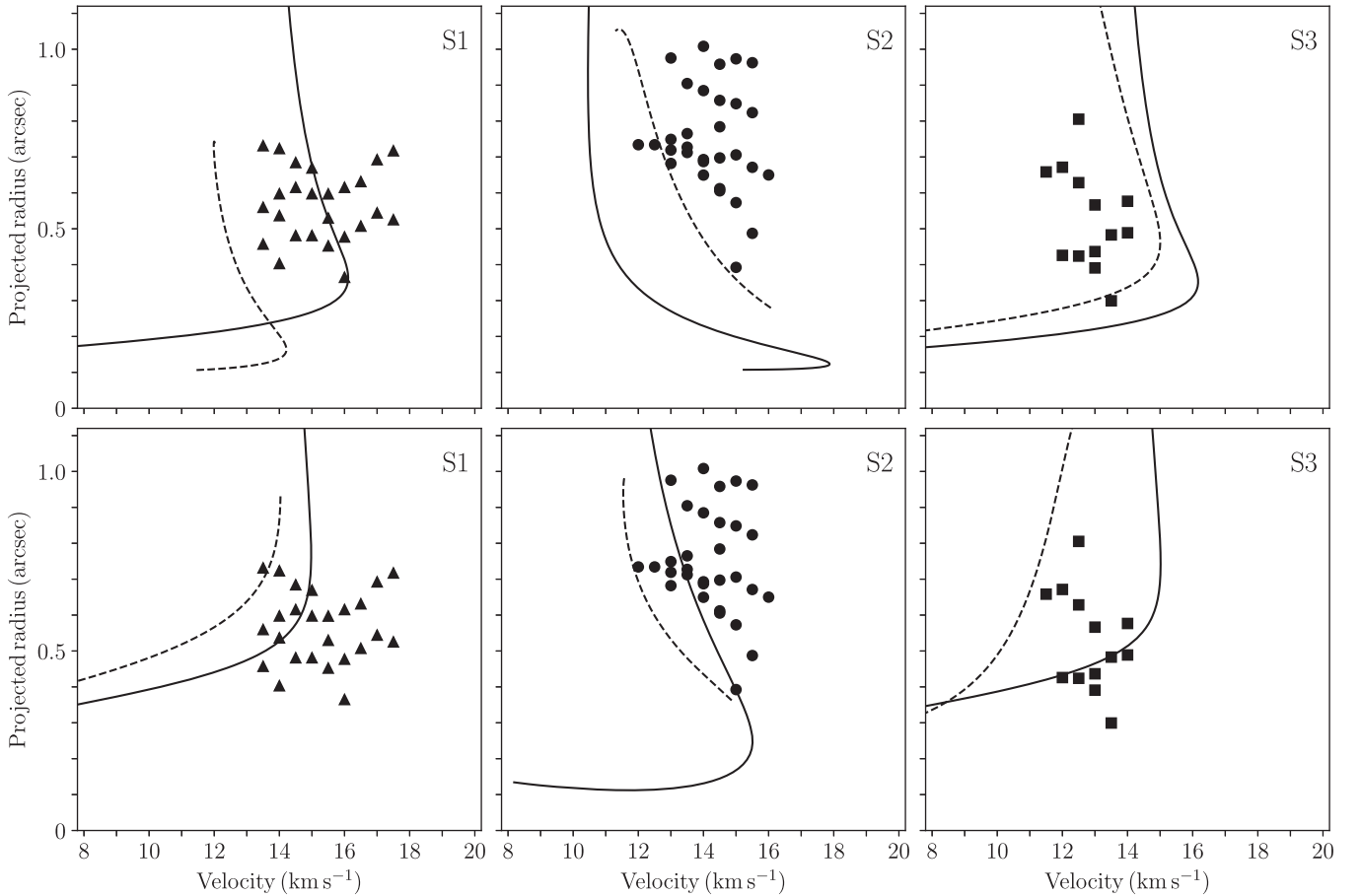


Figure 11. The CH_3OH position–velocity diagrams along the streamers S1, S2, and S3 (i.e., observed line-of-sight velocity vs. projected distance to the protostar location) for our best fits to the data using Ulrich’s model (solid lines) and Mendoza’s model (dashed lines). Note that the system velocity is 12.1 km s^{-1} . Top panels: using r_{in} as the molecular disk radius. Bottom panels: using r_{in} as the envelope radius. The triangles, circles, and squares correspond to the S1, S2, and S3 streamers, respectively.

In Section 4.5, we estimated the rate at which the dust disk is replenished with material from the hot molecular disk in $\sim 5 \times 10^{-4} M_{\odot} \text{ yr}^{-1}$. This rate implies an increase in the mass of the disk to $1 M_{\odot}$ in $\sim 2000 \text{ yr}$, which is currently estimated to be $5 M_{\odot}$ (Añez-López et al. 2020). This rate is 1 order of magnitude larger than the accretion rate onto the protostar estimated by Añez-López et al. (2020) ($7 \times 10^{-5} M_{\odot} \text{ yr}^{-1}$), meaning that the infalling material is bottlenecked onto the disk and may stay in the compact disk for $\sim 15,000 \text{ yr}$, orbiting the central object(s). This can explain the formation of a massive disk, which may have time to form gravitational instabilities. The accretion rate onto the compact disk would be lower if the solid angle of the accretion (as seen from the central protostar) is lower than that assumed here. One possible way is by feeding the compact dust disk asymmetrically (e.g., through streamers). However, the current angular resolution of the molecular data is not enough to discern if the detected streamers carry material below $\sim 360 \text{ au}$ from the protostar(s).

5.2. Central Absorption

Figure 14 shows how different molecules have absorption peaks at slightly different velocities at the center of the GGD 27-MM1 system. The absorption is not detected at large velocities expected in the inner part of the rotating compact disk, indicating that it happens likely in colder and quiescent gas layers associated with the envelope. Redshifted absorption toward circumstellar disks or

massive hot cores has been interpreted as signposts of infall motions from actively accreting layers with colder gas than the continuum (e.g., Zapata et al. 2013; Beltrán et al. 2018, 2022). An alternative explanation is that line intensities could be suppressed due to a continuum over-subtraction, caused by the CH_3CN lines being marginally optically thick at the disk center. Regardless, in the case of GGD 27-MM1, the continuum at the inner disk is absorbed by the colder gas surrounding it. Interestingly, some of the accreting streamers shown in previous Section 4.3 (and other possible streamers not identified here, but whose presence is hinted from the molecular gas distribution of some species such as H_2CO or SO_2 and CH_3OH) end at the redshifted velocities of the absorption peaks. Assuming that the accreting streamers cover the central part of the disk, causing the detected absorption, the material may be just hovering over the disk surface.

To estimate the mean column density in the inner 210 au of the GGD 27-MM1 protostellar system, we take, as an informed value, the CH_3CN column density extracted from our fit of the $J=17-16$ ladder at the central pixel (Table 6): $7.0 \times 10^{16} \text{ cm}^{-2}$. We can compare this value with an average of the H_2 column density in this region, estimated using the density profiles given by Equation (3) in Añez-López et al. (2020): $3.1 \times 10^{26} \text{ cm}^{-2}$. Hence, we derive an abundance of CH_3CN with respect to H_2 in the range of 2×10^{-10} . This is a value about 2 orders of magnitude lower than the fractional

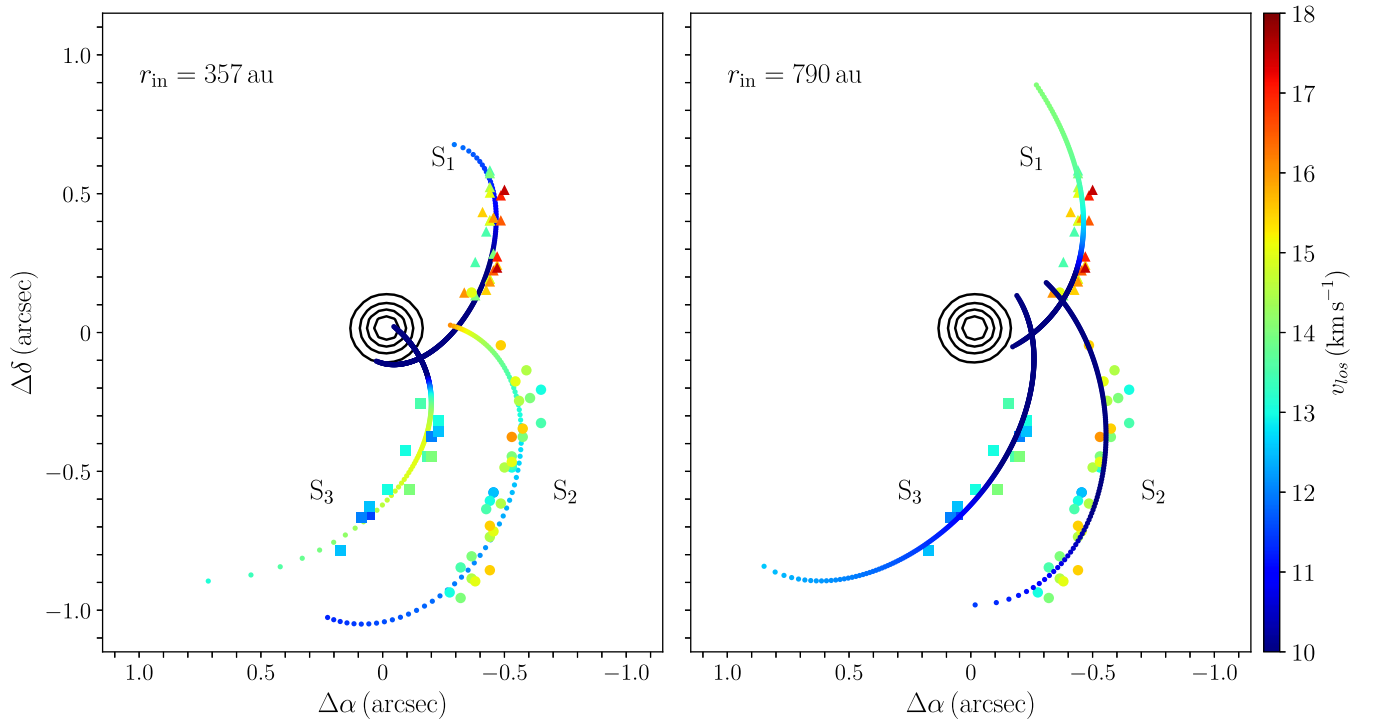


Figure 12. Trajectories of the S1, S2, and S3 streamers on top of the contours marking the strongest continuum emission. The line-of-sight velocity of the streamers for our best fit to the CH_3OH data using Mendoza’s model is also depicted (color scale). Left panel: using r_{in} as the molecular disk radius. Right panel: using r_{in} as the envelope radius. The triangles, circles, and squares correspond to condensations of the S1, S2, and S3 streamers and the colors follow the same velocity color scale as the model trajectories.

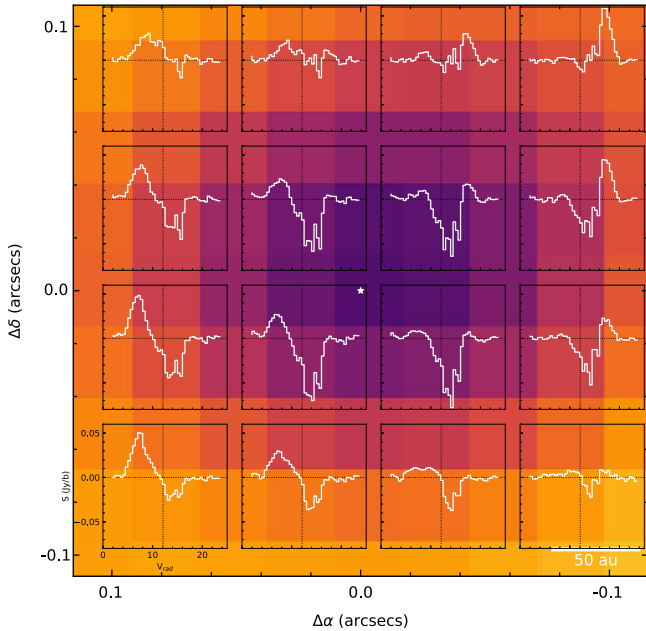


Figure 13. H_2S integrated intensity image (moment 0) of the inner region of the GGD 27-MM1 disk. The color scale shows the negative absorption toward the center position. The figure shows H_2S $3_{3,0}\text{--}3_{2,1}$ spectra extracted and overlaid every quarter of a beam, approximately. The star marks the position of the peak of the millimeter continuum emission.

abundances estimated toward several hot molecular cores ($\sim 10^{-8}$, e.g., Hernández-Hernández et al. 2014; Liu et al. 2020), and about 1 order of magnitude smaller than that found in the Orion hot core ($10^{-10}\text{--}10^{-9}$ Wilner et al. 1994; Bell et al.

2014). If this means that the abundance of the gas decreases at the center, it can explain why the inner regions of the disk do not display the Keplerian pattern of rotation expected at higher velocities (or why CH_3CN transitions with higher energy levels or even vibrational transitions were not detected at these high velocities). As commented before, the reasons behind this low abundance are unknown and we can only hypothesize about processes such as photoionization and/or radiation pressure. There is also the possibility of a continuum over-subtraction due to radial variations of temperature and opacity of the lines and the continuum. Further experiments probing atomic and/or infrared rovibrational transitions from the simplest molecules—such as CO—that may have escaped destruction, are needed to give more insight in this respect. Also, a good knowledge of the radial profile of the dust temperature and opacity, through detailed multiwavelength observations, can help to test the continuum over-subtraction effect.

5.3. Hot Molecular Disk

The current data hints at the possibility that several accretion streamers channel material that infalls onto the molecular disk (e.g., Figures 2 and 10). We estimate a large accretion/infall rate ranging between 10^{-3} and $10^{-2} M_{\odot} \text{yr}^{-1}$. For this estimate, we consider that the infalling solid angle is the flared region of 22° surrounding the midplane of the disk. If the presence of gas streamers means that the infall is channeled through them, the solid angle from the protostar depends on the section of the streamers at the distance of the deposition and the number of the streamers. The current data do not allow us to clearly resolve the width of the streamers. Hence, assuming a $0''.15$ width (the geometrical size of the beam), the solid angle for one

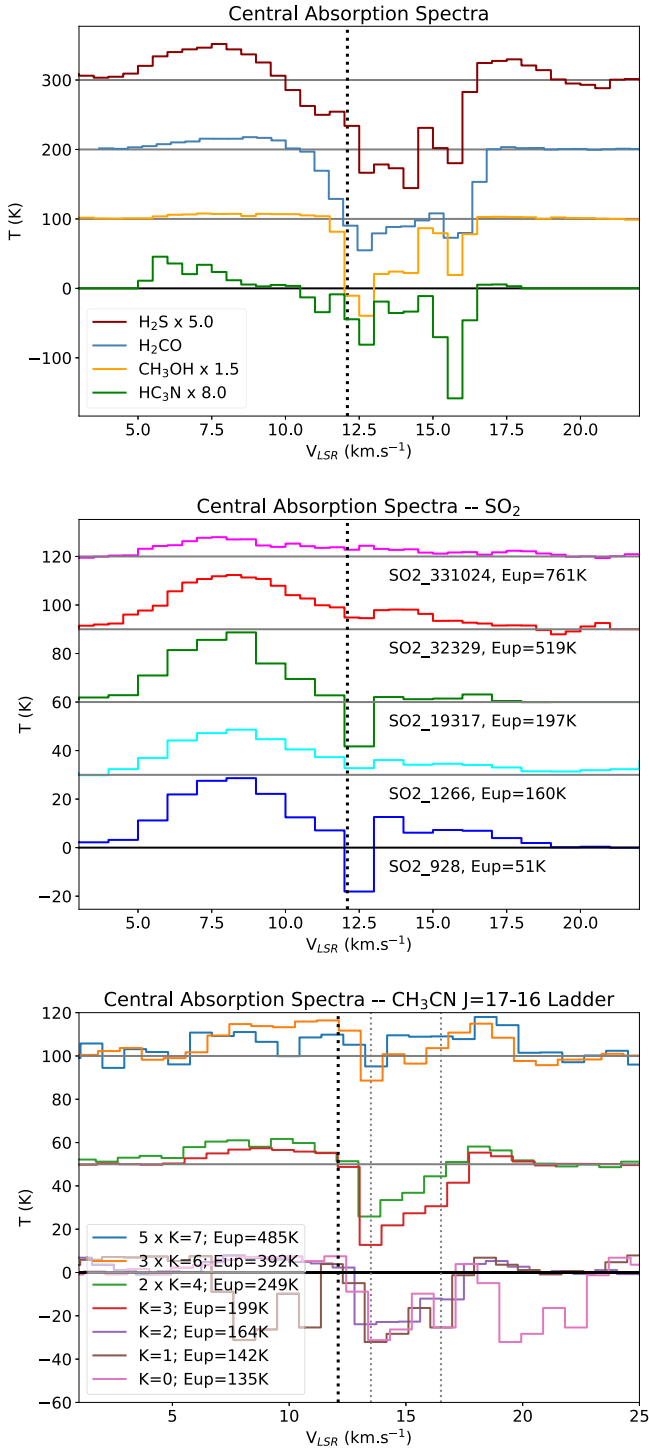


Figure 14. Spectra of different molecular transitions integrated over the central absorption region. The dotted black line in all the panels marks the 12.1 km s^{-1} systemic velocity. Top: H_2S , H_2CO , CH_3OH , and HC_3N lines. Middle: SO_2 lines with E_{up} ranging between 51 and 761 K. Bottom: several lines of the $\text{CH}_3\text{CN } J=17-16$ ladder. To help the readability some spectra are shifted in the y-axis, and some are also multiplied by an integer factor indicated in the legend. The two gray dotted lines mark the velocity of the two main absorption peaks at 13.5 and 16.5 km s^{-1} , see the main text.

streamer decreases by a factor of 3–10 relative to the solid angle of the flared disk. This factor is compensated by the number of streamers. Therefore, with the present data constraints, we can assume that the infall of material from the outskirts onto the disk may proceed very quickly.

Table 6
CH₃CN Central Pixel Spectral Fitting

Spectral Component	$N_{\text{CH}_3\text{CN}}$ (cm^{-2})	T_{ex} (K)	V (km s^{-1})	ΔV (km s^{-1})
Dust disk ^a	...	300
Gas disk	$7 \pm 1 \times 10^{16}$	480 ± 190	9.8 ± 0.1	5.8 ± 0.7
Envelope	$3.5 \pm 0.3 \times 10^{15}$	150 ± 40	13.7 ± 0.5	3.0 ± 0.5

Note.

^a Optically thick background emission source at a fixed uniform temperature assumed to be between 250 and 450 K. Note that this background temperature has a big uncertainty and needs to be fine-tuned for a more detailed analysis. The uncertainties of the free parameters are estimated taking into account the fits at the two background temperature extremes.

5.4. Warm Gas Envelope

The warm envelope is seen at quiescent velocities ($< 4 \text{ km s}^{-1}$), which are consistently redshifted with respect to the disk central velocity of 12.1 km s^{-1} derived in the kinematic analysis of the disk rotating pattern (e.g., Fernández-López et al. 2011b; Girart et al. 2017). If the material from the envelope is gravitationally bound¹³ in the potential well of GGD 27-MM1, then the fact that we only see redshifted emission can be explained by the disk being at the background edge of the original dense pocket. This pocket of material may be infalling onto the central system. Another redshifted-only envelope has been seen in RU Lup (Huang et al. 2020), and for example, the HH 30 protostellar system is known to be at the edge of its dense cloud (Louvet et al. 2018).

5.5. Possible Accretion Streamers Feeding GGD 27-MM1

Accretion streamers have lately been reported to channel material into low-mass young stellar systems from all evolutionary stages (see Pineda et al. 2023, and references therein for a current review). The structures found in GGD 27-MM1 match the expected shape, length, and kinematics shared by most of these streamers (as showed by our fitting), suggesting that the accretion process from large scales continue asymmetrically beyond the formation of a massive protostar and its massive disk. In principle, an asymmetric infall of material could be regarded as a slower accretion process (that is, considering two scenarios with the same flux of material through a fixed solid angle, infall through a few small cones will provide a slower accretion rate—less accretion—than isotropic infall), but if instead of the isotropic process, accretion is carried out via a relatively small flare angle (i.e., the infalling solid angle is just a portion of the whole spherical surface), and if there are several wide enough accretion streamers, the subtended angle of the accretion could be even larger than in the case of a flared isotropic accretion.

The analysis in Section 4.3 shows the plausibility that the filament-like structures extending outward from the molecular disk/envelope of the GGD 27-MM1 system could be accretion streamers. Both the morphology and the kinematics are qualitatively fitted by our modeling (Figures 10–12). The model using Mendoza’s paradigm of three streamers carrying material down to the envelope radius agrees especially well with the spatial distribution of the data. On the contrary, Ulrich’s model does

¹³ The escape velocity at 790 au, the radius of the envelope, is $4.7\text{--}6.7 \text{ km s}^{-1}$ for a central mass of $10\text{--}20 M_{\odot}$.

not work as well, rejecting the more static scenario proposed by this second model. Note, however, that from the line-of-sight velocities (Figure 11), it is not obvious which model is better. The other relevant result is that using Mendoza’s model, the current data do not allow to discern the endpoint for the accretion streamers. That is, the accretion streamers could well transport material onto both the outskirts of the envelope and the molecular disk. With the current angular resolution and sensitivity, other fitting solutions are possible (e.g., using different end radii for the streamers), so the present fitting is shown here as a proof of concept for the accretion streamer hypothesis.

In addition, we have only used the three streamers that are most apparent in the data of the different molecules. However, the molecular protuberances to the north of the molecular disk and to the northeast of the envelope, along with the persistent redshifted emission toward the east (contrarily to the rotation disk pattern) could indicate that other accretion paths exist.

Finally, let us note that, even though the hypothesis of accretion streamers seems to be very likely in this system, alternative explanations for these structures cannot be ruled out. A fly-by event or a close encounter with another object could display tails and spiral arms on large scales too (Kurtovic et al. 2018; Zapata et al. 2020; Cuello et al. 2023). A further analysis studying a wider field of view surrounding GGD 27-MM1 is currently ongoing, and its results will be shown in a forthcoming publication.

6. Conclusions

In this contribution, we have presented new ALMA 0.98 mm observations with an angular resolution of $\sim 0''.12$ toward the high-mass protostellar system GGD 27-MM1. The main results and final ideas of the paper are:

1. The continuum emission is well reproduced by a model including an unresolved central ionized source, a 190 au disk, a tenuous $0.2 M_{\odot}$ envelope, and two compact NW and NE components.
2. We mapped the emission of different SO_2 transitions, and CH_3OH , H_2CO , H_2S , HC_3N , and CH_3N lines. The different lines trace the molecular rotating disk, the envelope, and several arc-like structures, similar to the accretion streamers seen to feed material onto young stellar systems.
3. The H_2S line traces the molecular disk, seen as a crescent with a dim in the southern rim. We modeled its emission through an ad hoc model comprising a compact dust disk, whose emission is absorbed by the cold gas between the emitting lids of a flared molecular disk. The flared angle of the disk, extending between 140 and 360 au, is derived to be 22° .
4. We analyzed the emission from the CH_3CN (17–16) ladder with CASSIS, producing maps and radial profiles of the temperature, the column density, and the velocity for two different kinematical components: (i) the hot and rotating molecular disk, and (ii) the warm and quiescent redshifted envelope. We discuss that the redshifted envelope may be quiescently infalling onto the molecular disk, which may be located at the background end of its natal molecular pocket.
5. Regarding the possible presence of accretion streamers, a model of infalling gas with an initial nonzero velocity

toward the protostar (Mendoza’s model) seems to qualitatively fit the trajectories and line-of-sight velocities of three of these streamers. We, nevertheless, include an estimate of an isotropic accretion infall rate onto the disk through the flared angle of $\sim 5 \times 10^{-4} M_{\odot} \text{ yr}^{-1}$ at a 190 au radius, which is 1 order of magnitude larger than the accretion rate onto the protostar estimated by Añez-López et al. (2020). This may explain the formation of such a massive disk ($5 M_{\odot}$) in GGD 27-MM1.

6. The absorption toward the center of the system is detected at low velocities, and hence, it does not trace the disk rotation. It peaks at two or three different redshifted velocities depending on the transition, suggesting that may be related to different cold layers of gas. By fitting the CH_3CN spectrum, we found that material from the envelope is most likely producing the main absorption feature.
7. A relevant implication from the lack of emission/absorption detected at high velocities is the possible existence of a central zone, roughly coincident with the extent of the dusty disk, devoid of rapidly rotating molecular gas or hidden within the optically thick disk.

Acknowledgments

We thank the anonymous referee for a thorough and very constructive review that helped improve the consistency and quality of the paper. M.F.L. thanks the hospitality of the I.C.E. and the University of Barcelona; also the support from grant LACEGAL. J.M.G., R.E., and G.B. acknowledge support from the PID2020-11710GB-I00 grant funded by MCIN/AEI/10.13039/501100011033. S.C. acknowledges support from UNAM-PAPIIT IN103318 and IN104521 grants and from CONACyT, México. This work is also partially supported by the program Unidad de Excelencia María de Maeztu CEX2020-001058-M.

This paper makes use of the following ALMA data: ADS/JAO.ALMA#2015.1.00480.S. ALMA is a partnership of ESO (representing its member states), NSF (USA) and NINS (Japan), together with NRC (Canada), MOST and ASIAA (Taiwan), and KASI (Republic of Korea), in cooperation with the Republic of Chile. The Joint ALMA Observatory is operated by ESO, AUI/NRAO, and NAOJ.

Facility: ALMA.

Software: DS9 (Joye & Mandel 2003), CASA (v5.6.2 McMullin et al. 2007), Astropy (Robitaille et al. 2013), Karma (Gooch 1995), MAP (<http://sites.google.com/fqa.ub.edu/robert-estalella-home-page/map?authuser=0>).

Appendix A Continuum Fit

This section includes a visual comparison of the observed continuum emission and the model used to fit it in Section 3.1. A residual image between both is also presented in Figure 15. The fit of the central source still leaves residuals above 20σ , while removing the bulk of the central $>2500\sigma$ emission.

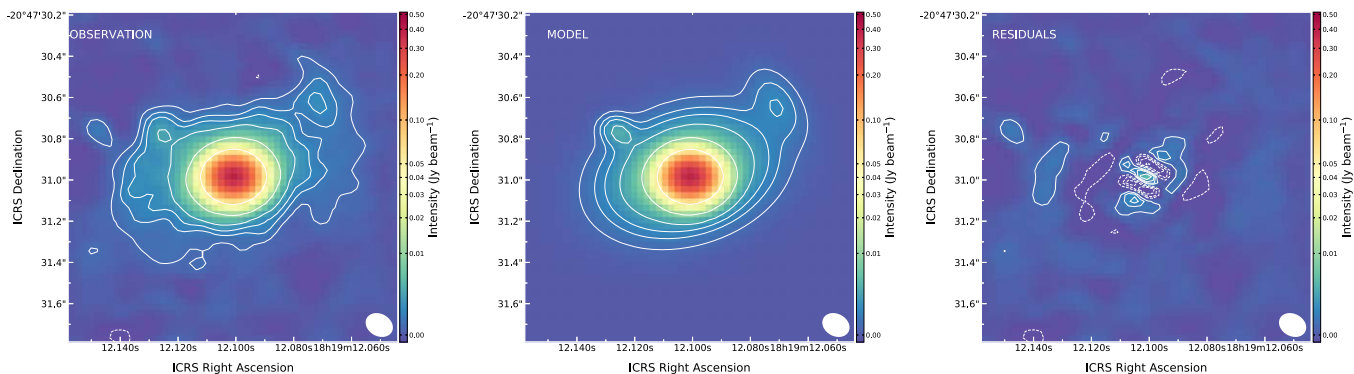


Figure 15. Continuum model for the continuum emission. From left to right, the images show the observed image, the model obtained, and the residual image after the fit. The three images have the same color scale and contours, at levels -25 , -10 , -5 , 5 , 10 , 15 , 25 , 75 , and 375 times the rms noise level of the image, ~ 0.14 mJy beam $^{-1}$.

Appendix B Velocity Cubes

This section contains velocity cube images with the emission of the lines presented in this paper: $\text{H}_2\text{S}(3_{3,0}-3_{2,1})$, $\text{HC}_3\text{N}(33-32)$, $\text{H}_2\text{CO}(4_{1,3}-3_{1,2})$, $\text{CH}_3\text{OH}(3_{1,2}-2_{0,2})$, $\text{SO}_2(9_{2,8}-8_{1,7})$, and $\text{CH}_3\text{CN}(17_3-16_3)$ (Figures 16–21). The field of view is a zoom-in to show the details of the disk and envelope toward GGD 27-MM1.

Enlarged versions of these figures may be presented in a forthcoming contribution. All of these figures show the ALMA Band 7 continuum emission overlapped with contours at 5, 15, and 100 times the rms noise level of the continuum emission ($140 \mu\text{Jy beam}^{-1}$). Details of each observed transition can be found in Table 1.

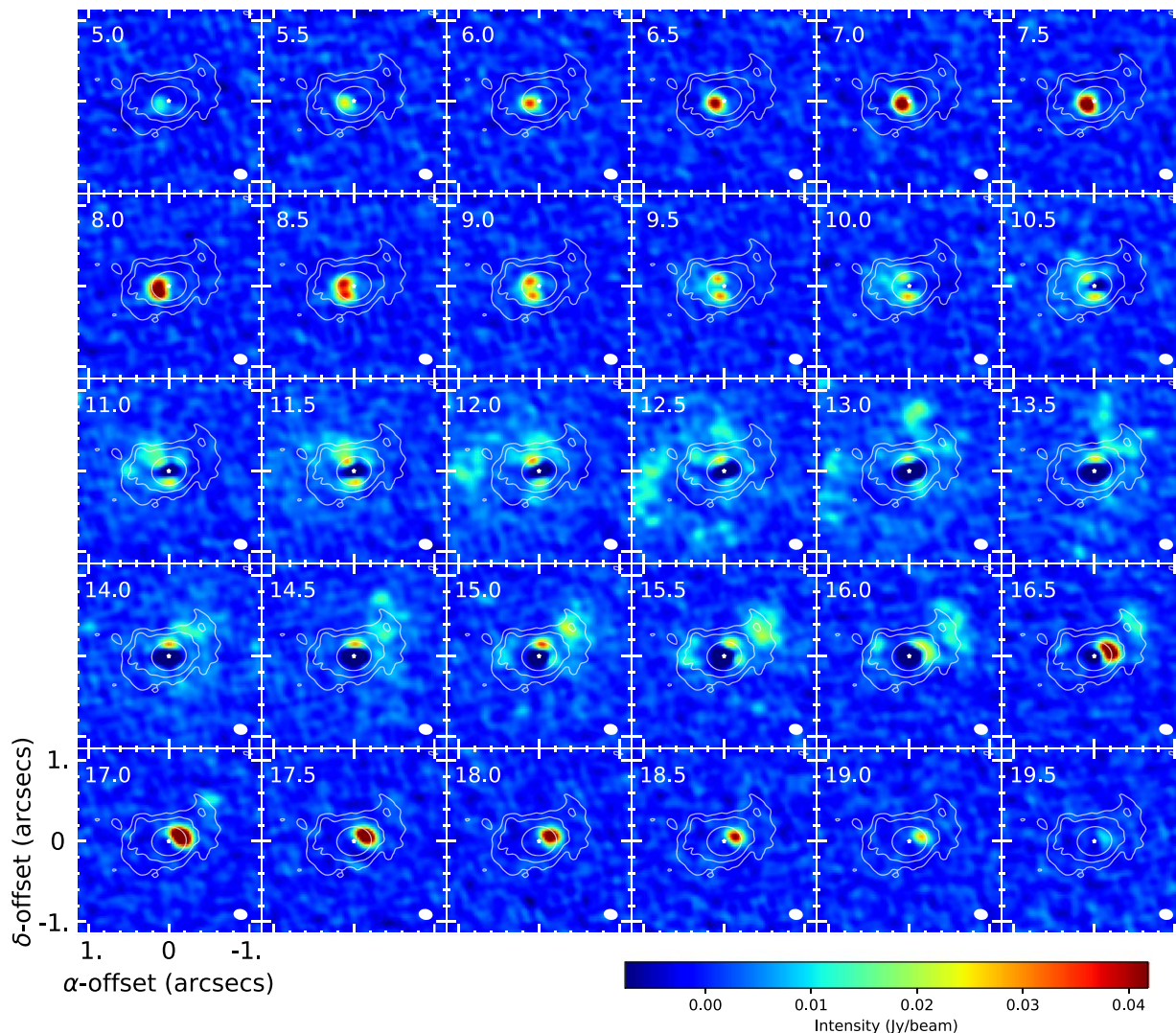


Figure 16. Zoom-in of the velocity cube image of the $\text{H}_2\text{S}(3_{3,0}-3_{2,1})$ emission toward GGD 27-MM1. Velocity is labeled in the top left corner and the synthesized beam appears in the bottom right corner of each channel. Band 6 continuum emission contours are overlapped at levels 5, 15, and 100 times the rms.

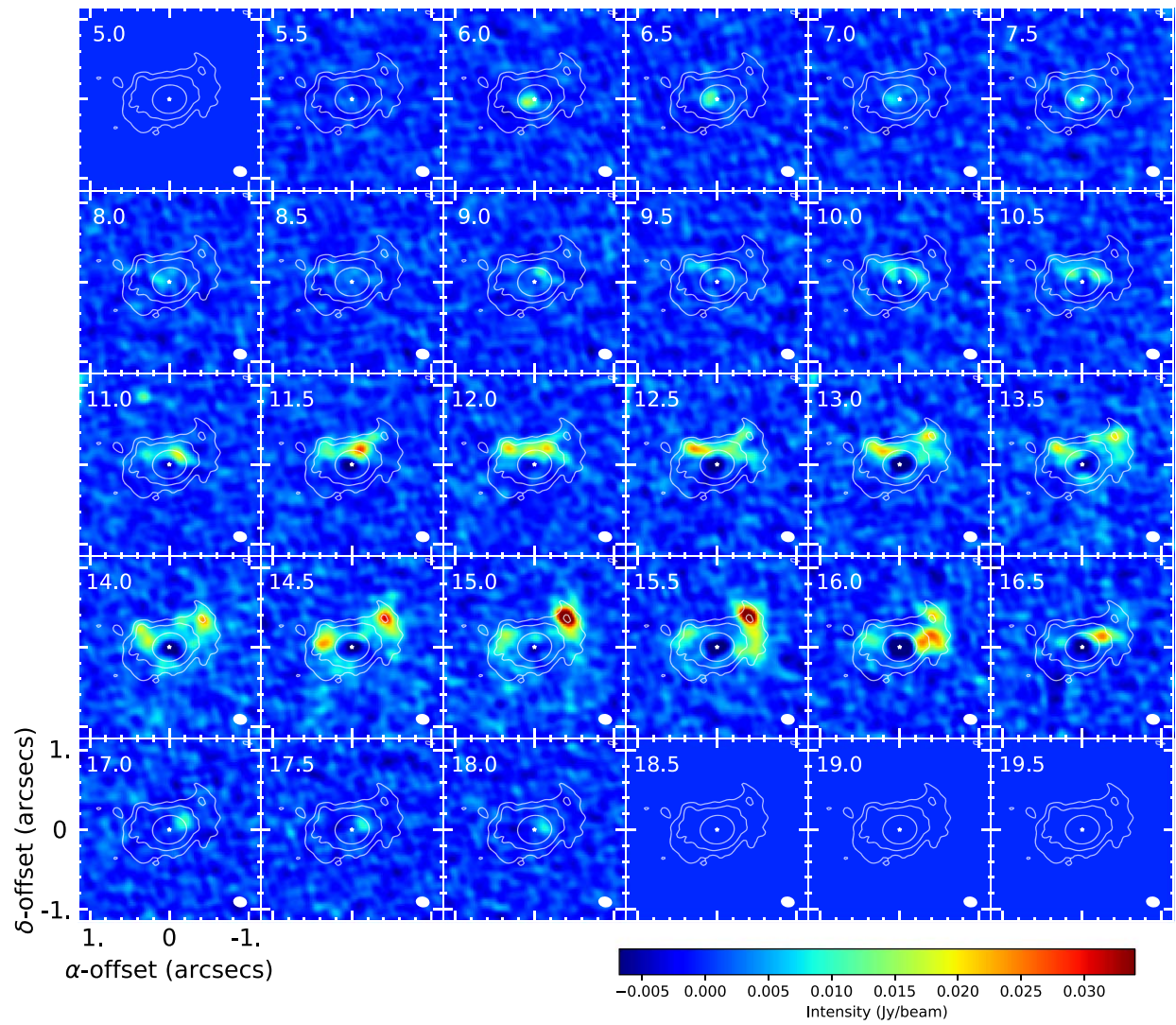


Figure 17. Zoom-in of the velocity cube image of the $\text{HC}_3\text{N}(33-32)$ emission toward GGD 27-MM1. Velocity is labeled in the top left corner and the synthesized beam appears in the bottom right corner of each channel. Band 6 continuum emission contours are overlapped at levels 5, 15, and 100 times the rms.

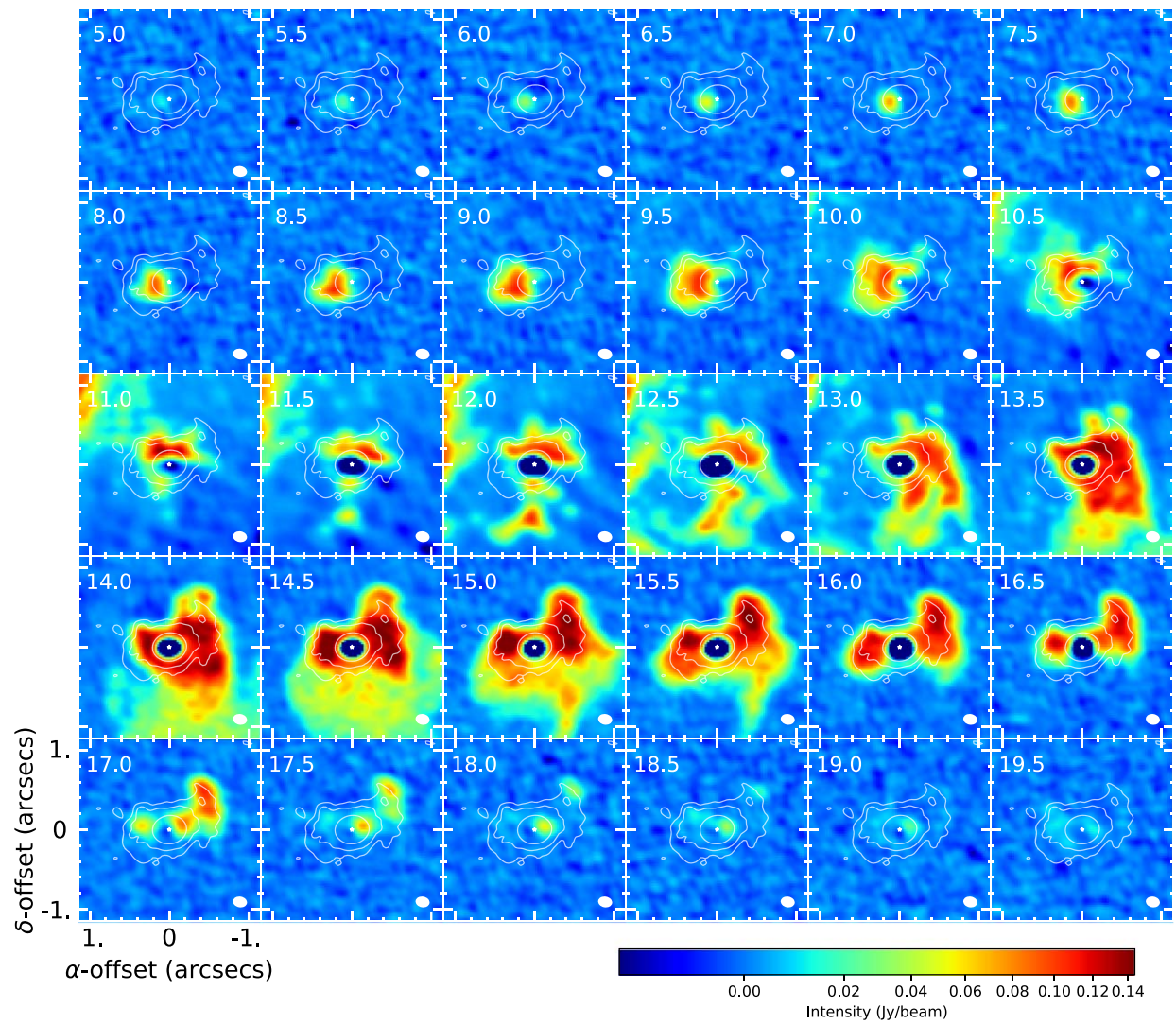


Figure 18. Zoom-in of the velocity cube image of the H_2CO ($4_{1,3}-3_{1,2}$) emission toward GGD 27-MM1. Velocity is labeled in the top left corner and the synthesized beam appears in the bottom right corner of each channel. Band 6 continuum emission contours are overlapped at levels 5, 15, and 100 times the rms.

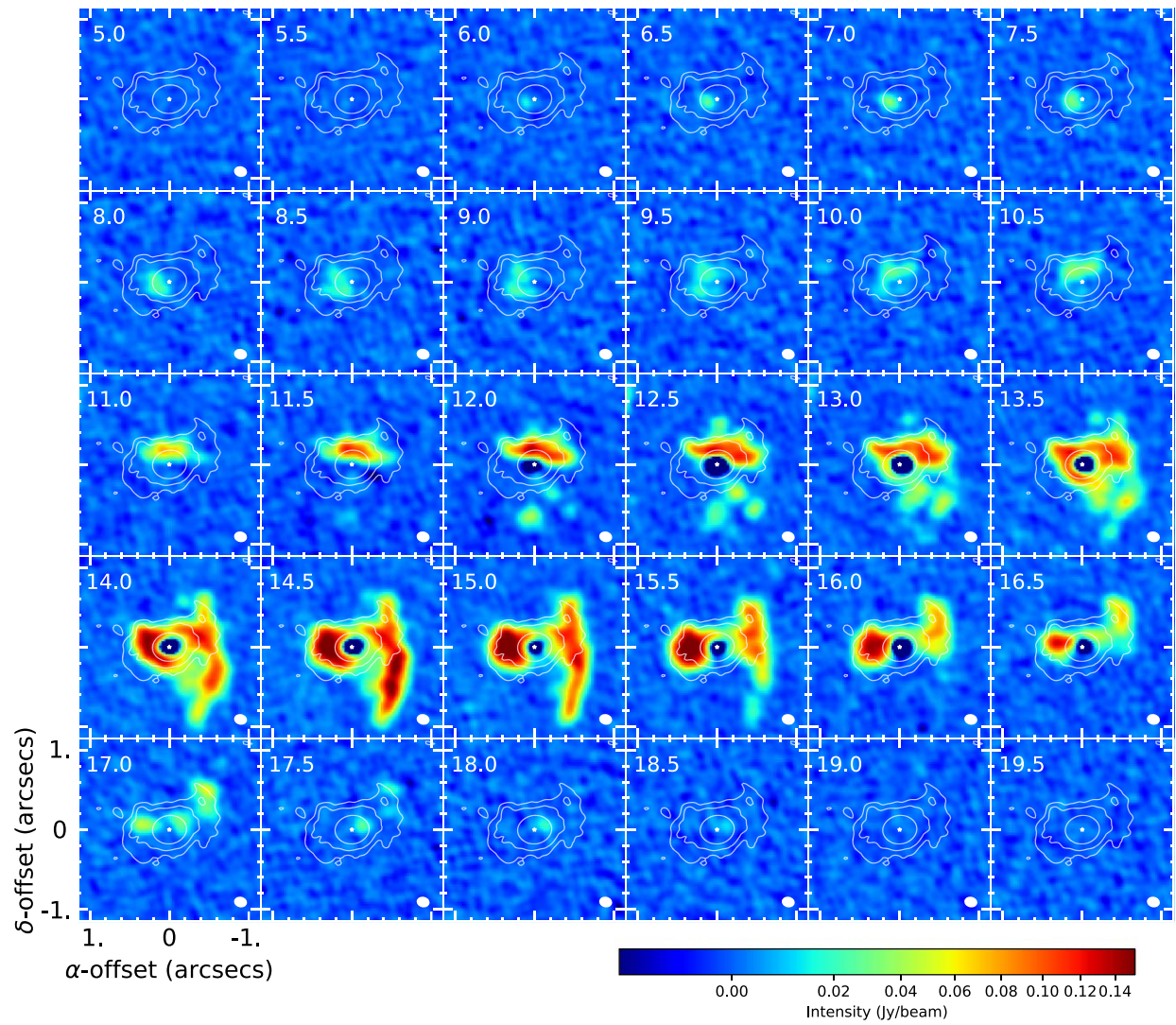


Figure 19. Zoom-in of the velocity cube image of the CH_3OH ($3_{1,2}-2_{0,2}$) emission toward GGD 27-MM1. Velocity is labeled in the top left corner and the synthesized beam appears in the bottom right corner of each channel. Band 6 continuum emission contours are overlapped at levels 5, 15, and 100 times the rms.

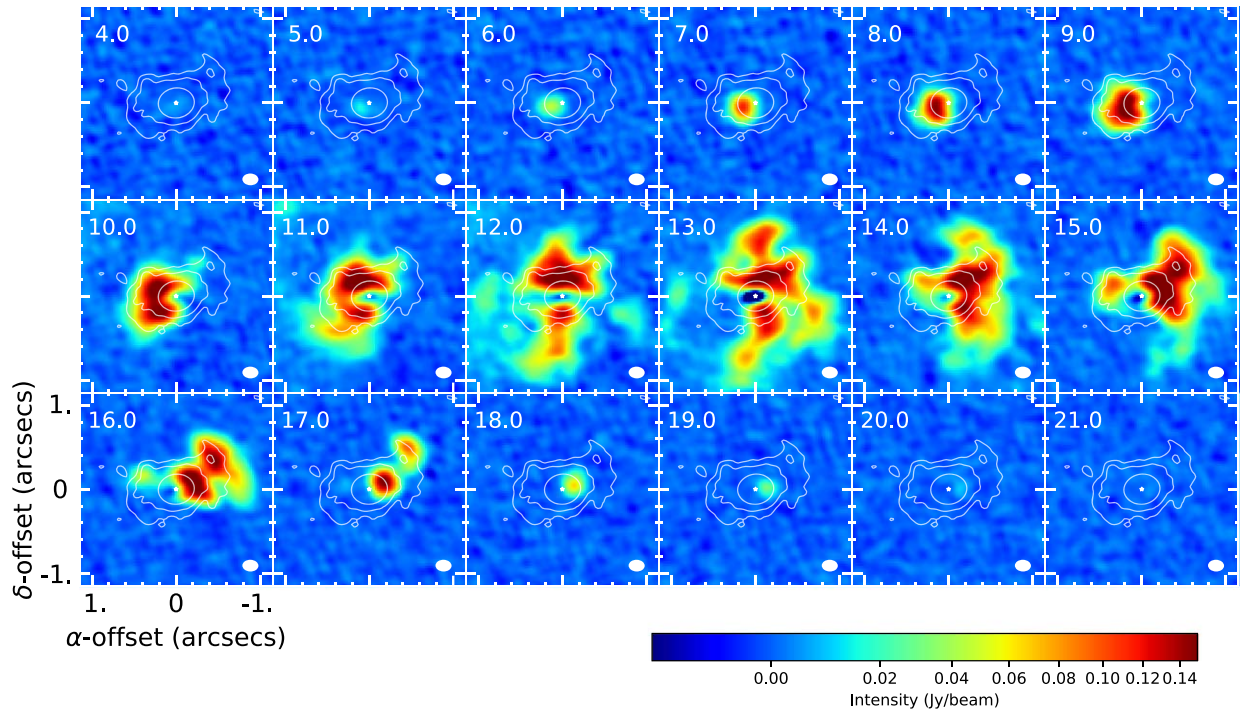


Figure 20. Zoom-in of the velocity cube image of the $\text{SO}_2(9_{2,8}-8_{1,7})$ emission toward GGD 27-MM1. Velocity is labeled in the top left corner and the synthesized beam appears in the bottom right corner of each channel. Band 6 continuum emission contours are overlapped at levels 5, 15, and 100 times the rms.

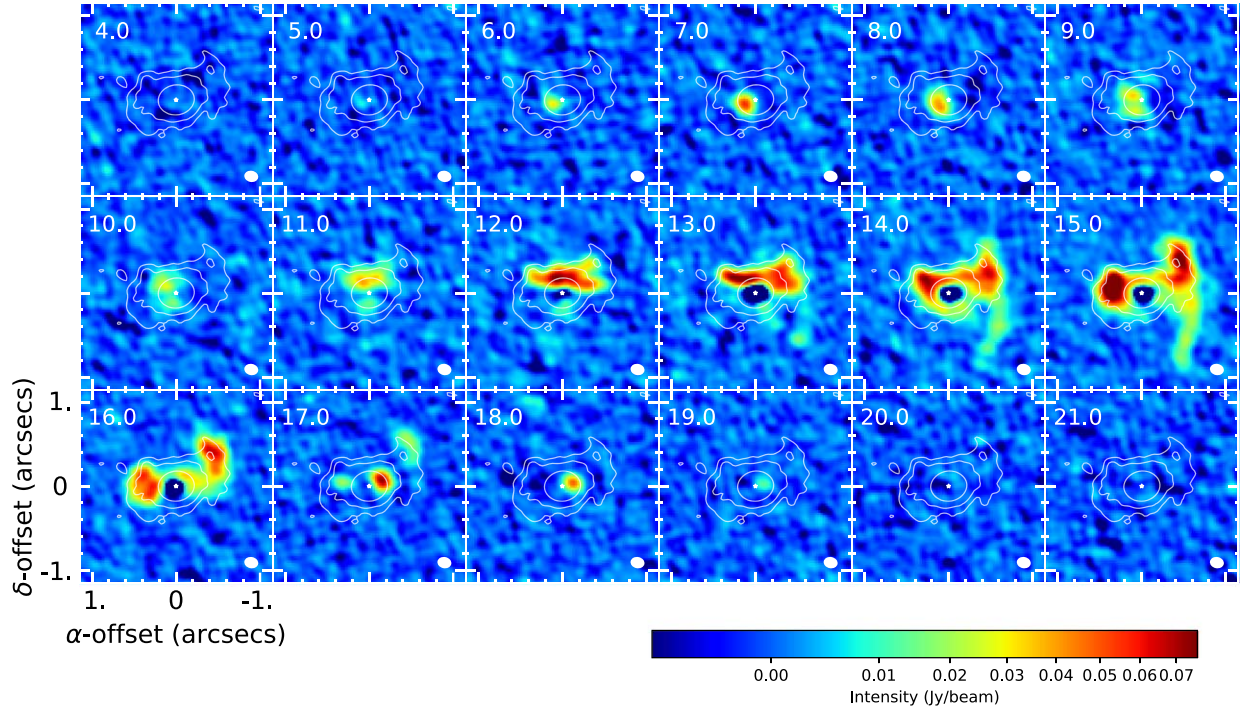


Figure 21. Zoom-in of the velocity cube image of the $\text{CH}_3\text{CN}(17_{3-16_3})$ emission toward GGD 27-MM1. Velocity is labeled in the top left corner and the synthesized beam appears in the bottom right corner of each channel. Band 6 continuum emission contours are overlapped at levels 5, 15, and 100 times the rms.

Appendix C

T_k and $N_{\text{CH}_3\text{CN}}$ Fitting Procedure Using CASSIS

We analyzed the CH_3CN data using CASSIS (Vastel et al. 2015). For each beam-sized pixel we fit one or two spectral components manually, except for the central pixel (see Figures 22–24). We take into account lines with peaks over the 4σ level ($\sigma = 0.72$ K), avoiding the $K = 5$ transition, whose

emission is blended with $\text{SO}_2(22, 4, 18-22, 3, 19)$. We fixed the size of all the spectral components as if they would fill the beam ($0''.15$) and set the telescope to ALMA with a 1300 m baseline. Our trials sample a range of excitation temperatures (10–600 K), column densities (8×10^{13} – 8×10^{15} cm^{-2}), line widths (0.1 – 5 km s^{-1}), and central velocities around the 12.1 km s^{-1} system velocity. We estimate that uncertainties may be 20 K for

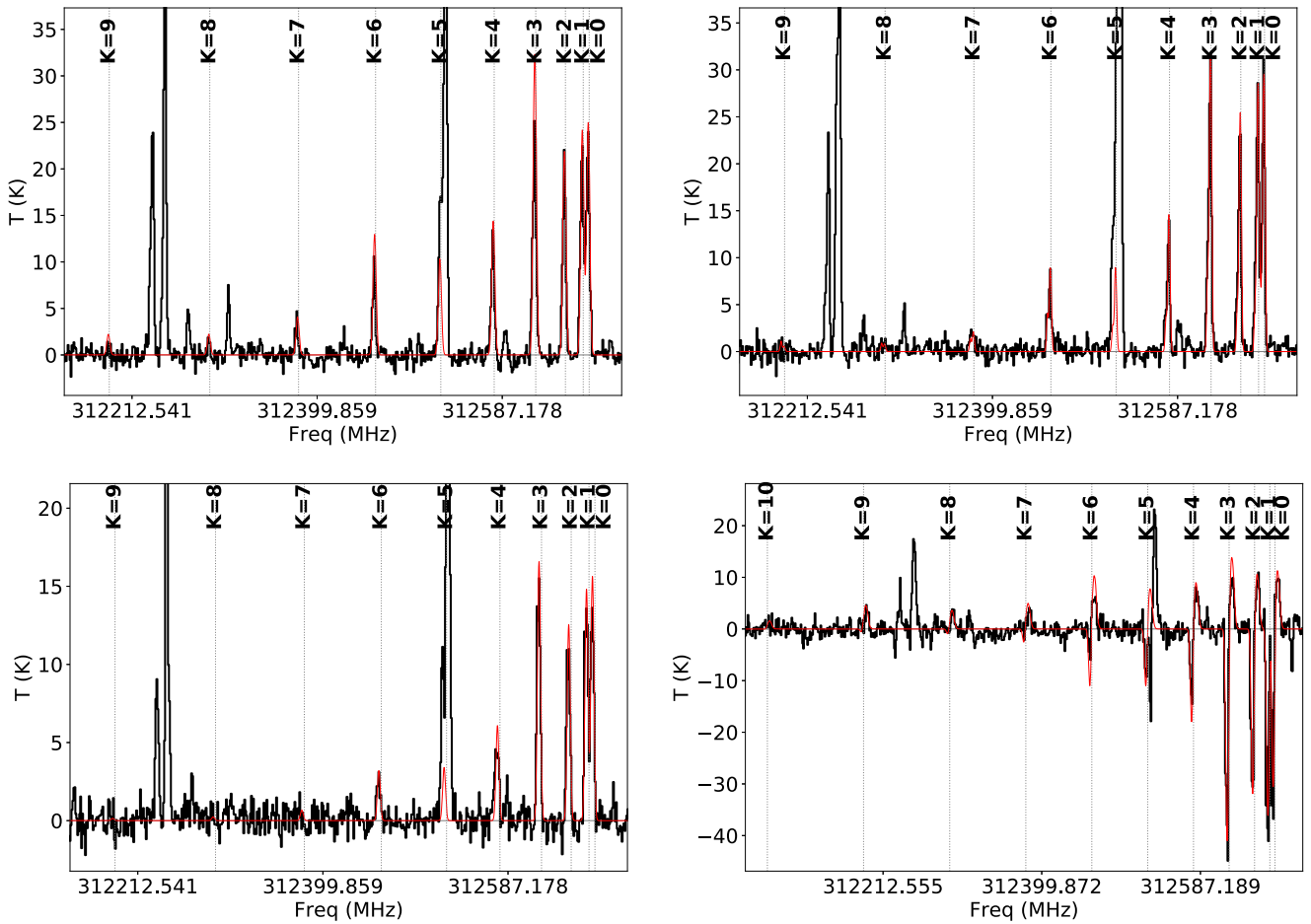


Figure 22. Example of spectra fitted manually using CASSIS (pixels 3–9, 4–9, 6–7, and that of the central pixel). The observed spectra are shown by the black histograms, while the CASSIS fitting is displayed by the red curves. The top and bottom left spectra are examples of fits obtained using a single kinematical component; the top right is a fit obtained using two spectral components; the bottom right spectrum corresponds to the central pixel spectrum, which was fit using a constant background of ~ 300 K, a blueshifted emitting layer and a foreground absorbing layer slightly redshifted. Note that CH₃CN $K = 5$ is contaminated by the SO₂ 22_{4,18}–22_{3,19} line ($\nu_{\text{rest}} = 312.543$ GHz). There are other strong lines (e.g., a CH₃OH line and a SO₂ line at about 312.24 GHz) in the spectra, which will be reported in another work.

the excitation temperatures, at 10%–20% in the CH₃CN column densities, and 0.1 – 0.25 km s^{−1} for both the line width and the offset velocities. The pixels with multiple spectral components have been fitted using a multicomponent approach (*interacting* layer in CASSIS). After all the pixels were fitted, we identified two

separate kinematical and temperature components (disk and envelope), used to construct maps of temperature, column density, and velocity for each component. The $K = 9$ ladder line is detected in several pixels. At the central pixel, even the $K = 10$ line is detected (Figure 22).

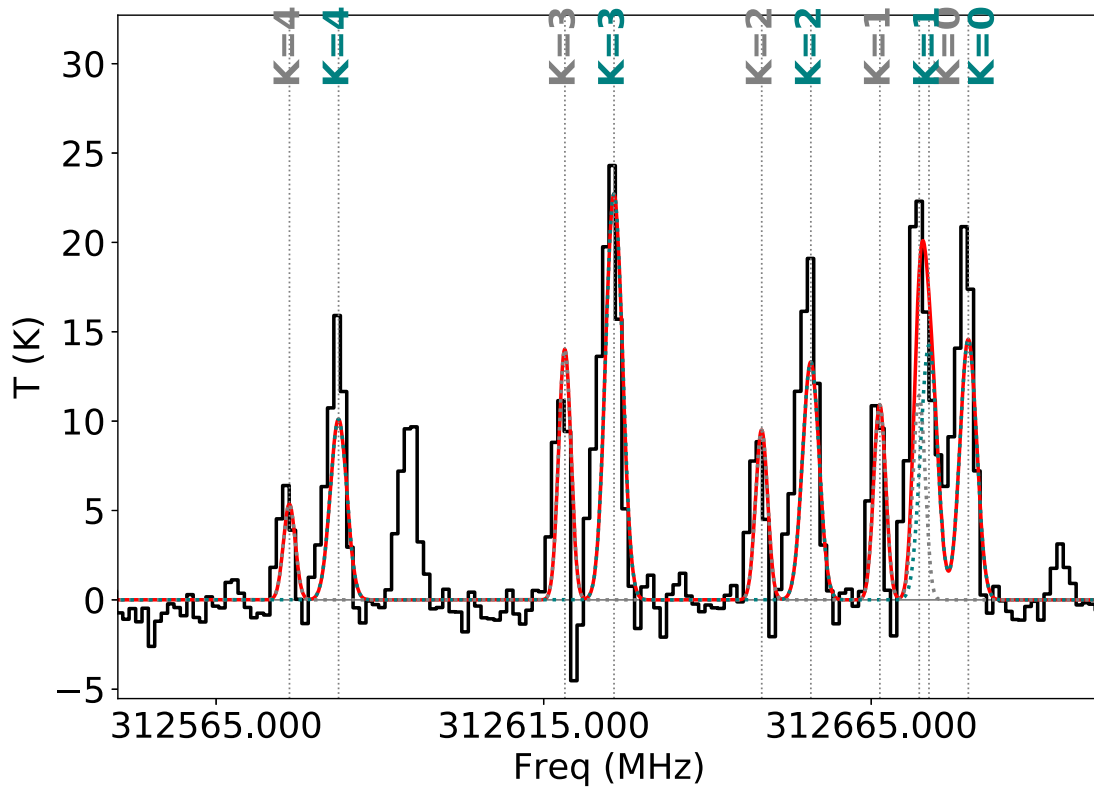


Figure 23. Zoom-in example of the up to $K = 4$ transition of the CH_3CN spectrum fitted manually using CASSIS (pixel 3–7). This demonstrates the need for two kinematical components and the relative goodness of the fit. The observed spectrum is shown by the black histogram, each of the two components has its spectrum plot in gray and blue dotted lines, and the red solid line represents the total fit after adding the two components' contributions.

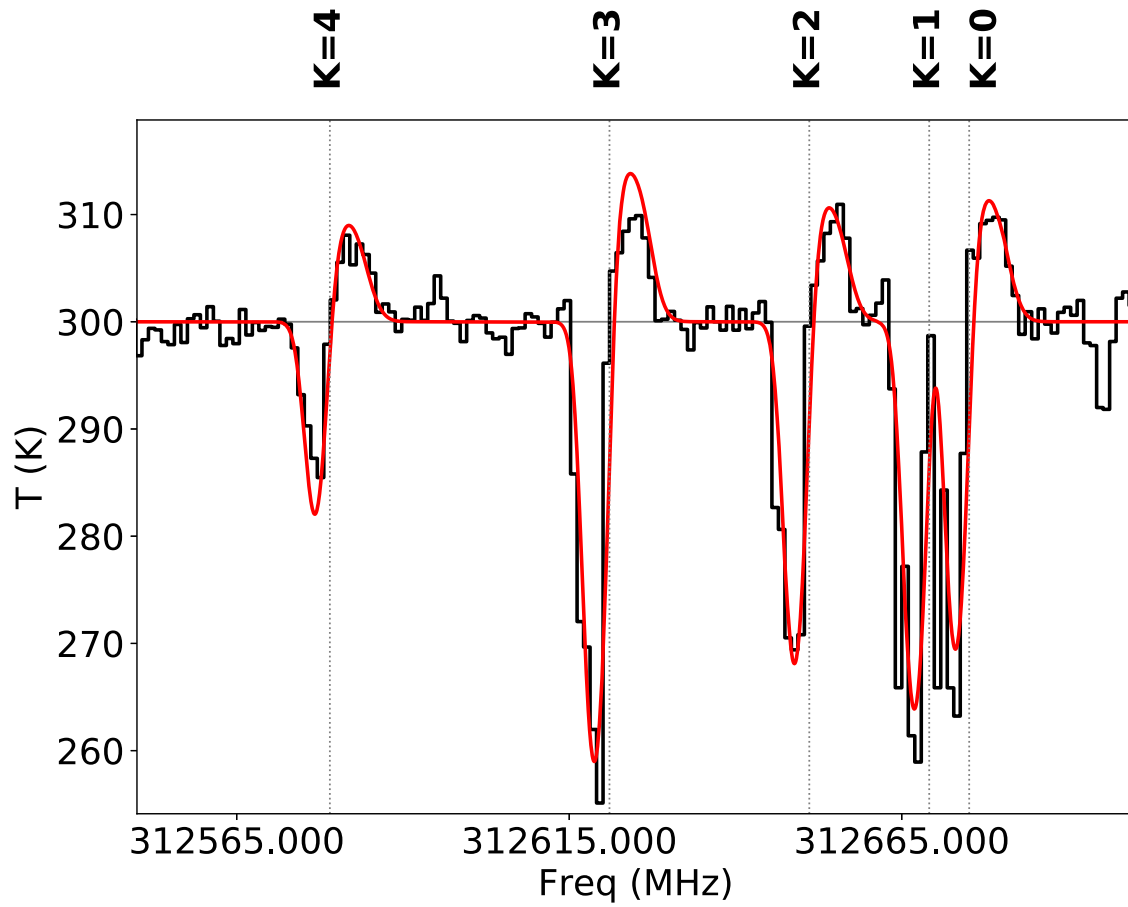


Figure 24. Zoom-in example of up to the $K = 4$ transition of the CH_3CN spectrum fitted manually using CASSIS at the central pixel. This demonstrates the relative quality of the fit fixing the background temperature at 300 K and using two interactive emitting/absorbing layers. The observed spectrum is shown by the black histogram and the red line represents the model.

Appendix D Infall Model Comparison

The analytic accretion flow model for the material rotating and collapsing into a central gravitational object was presented by Mendoza et al. (2009). This model is an expansion of the model presented by Ulrich (1976); the differences are that the radius of the rigid body rotating cloud is finite and the particles on the border of the cloud, they can have a radial velocity component, that is, the velocity aim to the center of the coordinates system. Mendoza’s model depends on the two parameters associated with these differences, μ and ν . In such a way if these parameters are $\mu = 0$ and $\nu = 0$, Mendoza’s model converges with Ulrich’s model. Under these differences, Mendoza’s model produces orbits described by conic sections and Ulrich’s model produces parabolic orbits. If the infalling material does not shock with its counterpart or with the accretion disk, this material could return to the border of the cloud, following the trajectory described by a parabolic orbit or by the conic orbit.

Figure 25 presents the orbits projected onto the plane of the sky where we do not consider an inclination angle $i = 0^\circ$ and we plot all trajectories of the material, we use an initial polar angle of $\theta_0 = 30^\circ$ and different initial azimuthal angles, from $\phi_0 = 0^\circ$ to $\phi_0 = 300^\circ$ with a difference of 60° . In order to dimension these orbits, we assume the inner equatorial radius equal to the envelope radius, $r_{\text{in}} = 790$ au. The left panel

corresponds to the parabolic orbits in Ulrich’s model, and the right panel corresponds to the conic orbits in Mendoza’s model. For Mendoza’s model, we use the parameters $\mu = 0.45$ and $\nu = 0.15$, since these parameters are not zero, the conic orbits are smaller and more curved than the parabolic orbits because the radius of the cloud is smaller.

For the same parameters μ and ν , the same angle θ_0 , the initial azimuthal angles from $\phi_0 = 0^\circ - 240^\circ$ with a difference of 120° , and the same inner radius r_{in} , Figure 26 shows a comparison between both models. The solid lines represent the orbits of Ulrich’s model and the dashed lines are the orbits produced by Mendoza’s model. The left panel shows an orbit projected onto the plane of the sky for an inclination angle of $i = 0^\circ$ and the right panel presents orbits with an inclination angle of $i = 30^\circ$.

The models mentioned above can reproduce the streamers S1, S2, and S3 (see Figure 9) as shown in Figures 27 and 28. Ulrich’s model (solid lines) and Mendoza’s model (dashed lines) orbits are overlapped with the integrated intensity emission (moment 0) of $\text{CH}_3\text{OH } 3_{(1,2)}-2_{(0,2)}$ emission for different velocity channels. We use the parameters μ and ν and the angles ϕ_0 and θ_0 of Table 5. Figure 27 is for the inner equatorial radius of $r_{\text{in}} = 357$ au (the molecular disk radius) and Figure 28 is for $r_{\text{in}} = 790$ au (envelope radius). The triangles, circles, and squares in Figures 27 and 28 mark the position of the condensations identified in the CH_3OH velocity cube.

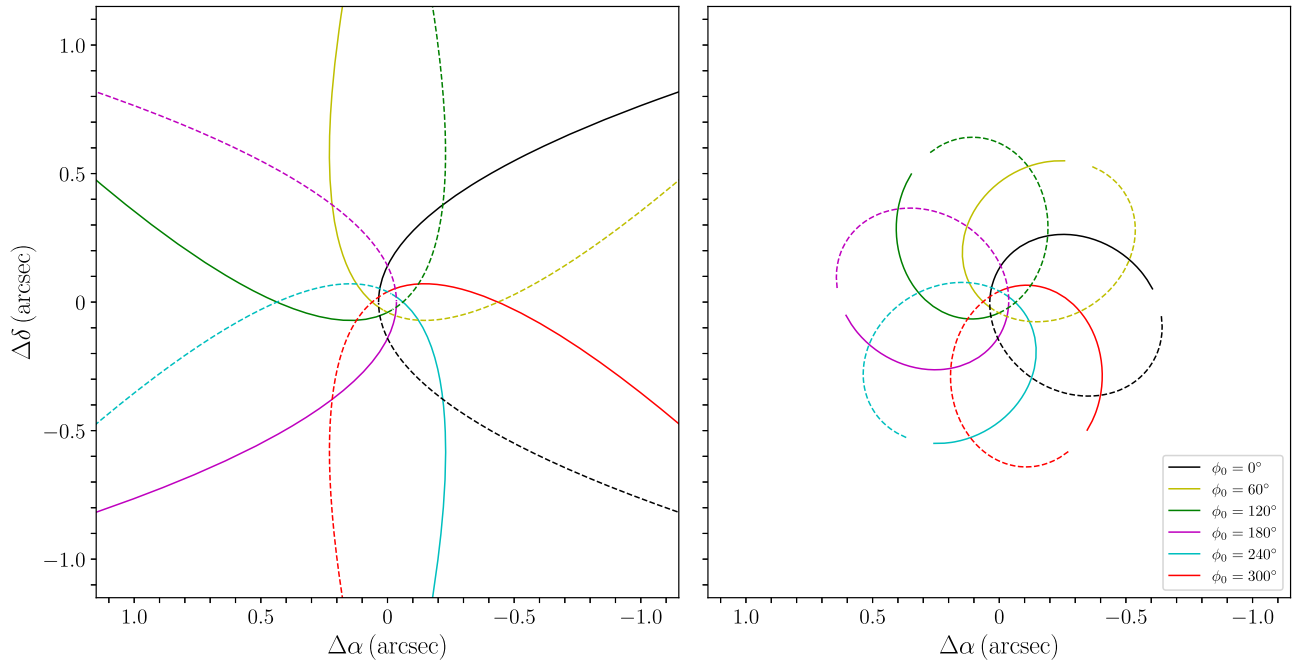


Figure 25. Comparison between the orbits projected onto the plane of the sky for an inclination angle $i = 0^\circ$, the inner equatorial radius r_{in} as the envelope radius (790 au), the initial polar angle $\theta_0 = 30^\circ$, and different initial azimuthal angles. Left panel: Ulrich’s model. Right panel: Mendoza’s model. For Mendoza’s model, we use the parameters $\mu = 0.45$ and $\nu = 0.15$. The solid lines represent the infalling material, while the dashed lines denote material coming out

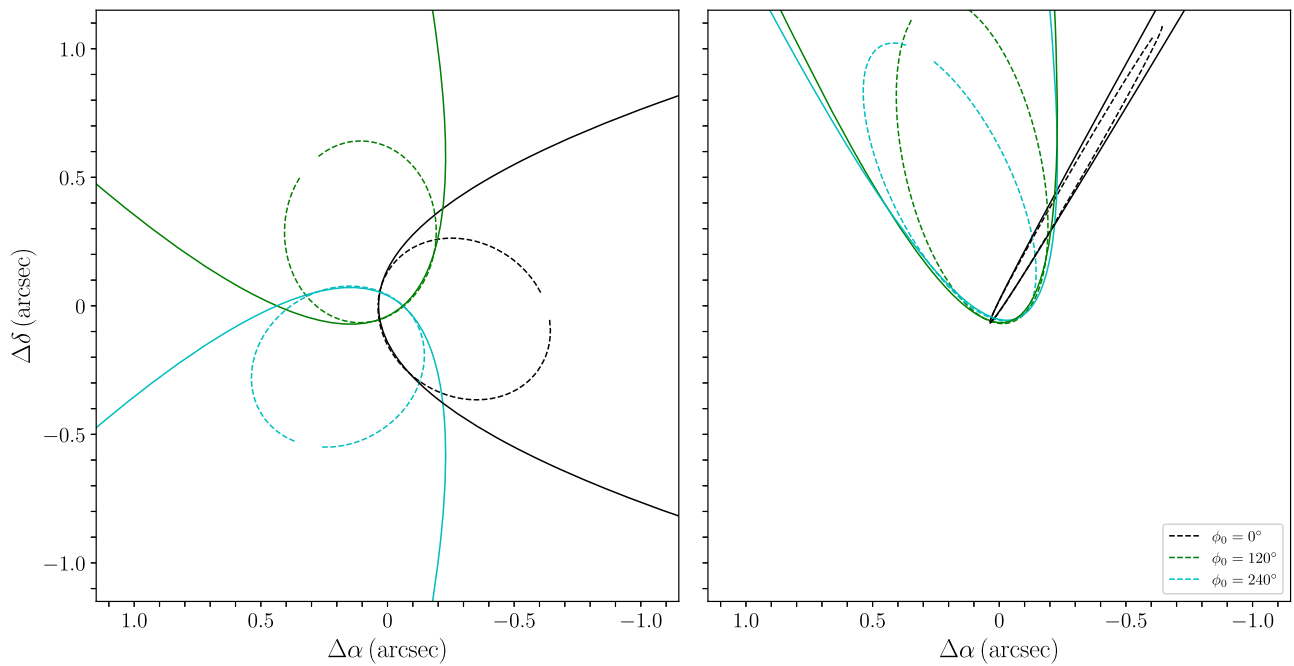


Figure 26. Comparison between the orbits projected onto the plane of the sky for an initial polar angle $\theta = 30^\circ$ and the envelope radius ($r_{\text{in}} = 790$ au). Parabolic orbits, following Ulrich's model are shown in solid lines. Conic orbits, following Mendoza's model are shown in dashed lines. Left panel: orbits for an inclination angle with respect to the plane of the sky $i = 0^\circ$. Right panel: orbits for an inclination angle with respect to the plane of the sky $i = 30^\circ$. For Mendoza's model, we consider the parameters $\mu = 0.45$ and $\nu = 0.15$.

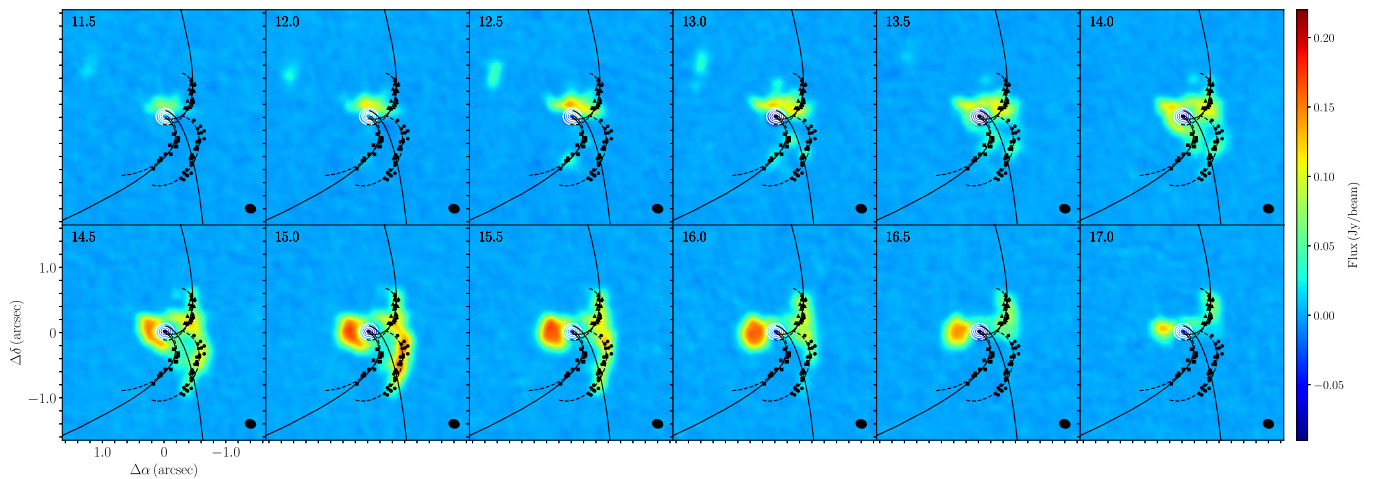


Figure 27. Ulrich (solid lines) and Mendoza (dashed lines) orbits overlapped with moment 0 of the $\text{CH}_3\text{OH } 3_{(1,2)}-2_{(0,2)}$ emission. The parameters μ and ν and the angles ϕ_0 and θ_0 for the streamers S1, S2, and S3 (see Figure 9) are shown in Table 5. The models use the inner equatorial radius r_{in} , as the molecular disk radius (357 au).

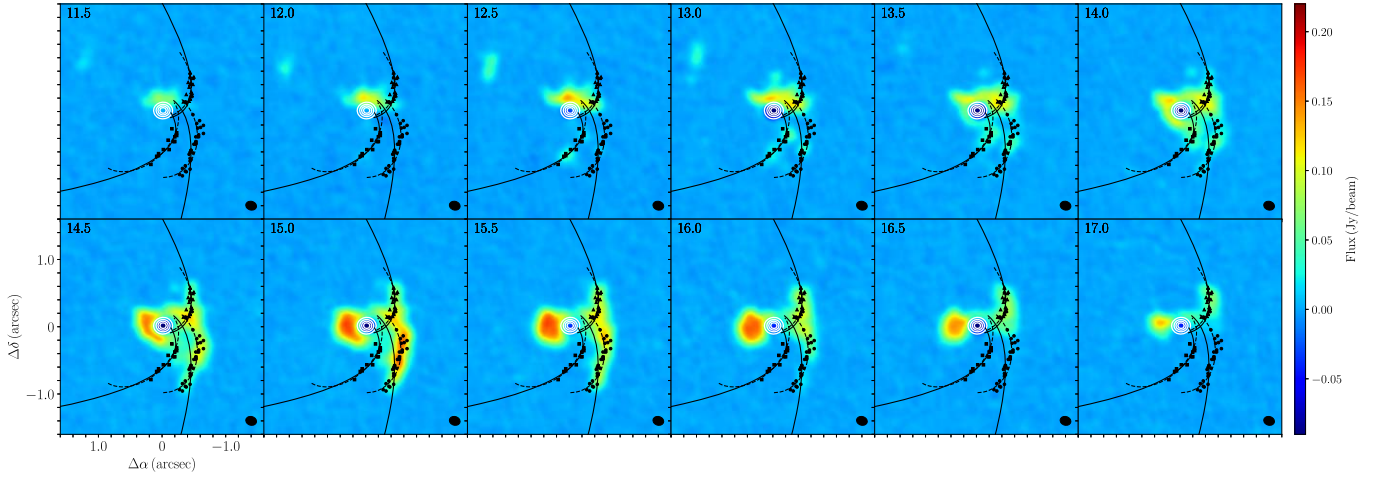


Figure 28. Ulrich (solid lines) and Mendoza (dashed lines) orbits overlapped with moment 0 of $\text{CH}_3\text{OH } 3_{(1,2)}-2_{(0,2)}$ emission. The same description as Figure 27 but models using the envelope radius $r_{\text{in}} = 790$ au.

Appendix E Flared Disk Model Details

In this section, we detail how the H_2S disk model is constructed. We are assuming a protoplanetary disk around a YSO, observed in some molecular transition, and we want to model the integrated intensity (zeroth moment) of the line. The disk has three different components: (i) a central dust disk, with a radius R_{dust} smaller than the inner radius of the molecular disk. It has no line emission, and is seen in absorption after subtracting the continuum emission; (ii) a molecular disk, which is flared and illuminated by the central YSO. Only the two faces of the disk are hot and have line emission. The flared disk extends from an inner radius R_{inn} to an outer radius R_{out} ; and (iii) cold gas that fills the volume of the flared disk, with a nonzero optical depth, responsible for the absorption of the continuum emission of the dust disk.

E.1. Model Parameters

The model depends on a number of six parameters describing the geometry of the system, and five describing the integrated intensities and optical depth. The geometrical parameters are:

θ : Position angle of the projection of the disk axis on the sky, i.e., of the minor axis of the ellipse projected on the sky.

With this definition, the position angle of the major axis of the ellipse is $90^\circ + \theta$.

i : Inclination angle of the disk, i.e., angle between the disk axis and the line of sight. For a face-on disk, $i = 0$.

R_{dust} : Radius of the dust disk. The dust disk is assumed to be flat, with a half-width of $H_{\text{dust}} = R_{\text{dust}} \tan \phi$.

$R_{\text{inn}}, R_{\text{out}}$: Inner and outer radii of the molecular disk.

ϕ : Flare angle of the molecular disk. The width of the disk increases linearly with radius. For a radius r , the half-height of the disk is given by $h = r \tan \phi$.

The parameters that describe the physical conditions of the disk are:

I_{dust} : Integrated intensity of the dust emission. The dust emission is assumed to be optically thick.

I_{face} : Integrated intensity of the face of the molecular disk.

I_{cold} : Integrated intensity of the cold gas, assumed to be uniform. The cold gas fills a cylindrical volume of radius R_{out} and half-width $H_{\text{cold}} = R_{\text{cold}} \tan \phi$.

τ_0 : Optical depth of the cold gas for a geometrical length R_{out} . For a given path-length l inside the cold gas, the optical depth is given by $\tau_0(l/R_{\text{out}})$.

E.2. Calculation of the Intensity

The model calculates, for every position of the model map, the intersections of the different disk components with the line of sight. The surfaces limiting the different components can be cylindrical (outer and inner sides of a disk), flat (top and bottom lids of a cylindrical disk), or conical (faces of a flared disk). For each one of these surfaces, the intersection with the line of sight is found.

For every position of the model map, once the intersections of the line of sight have been found, they are sorted from farthest to closest to the observer. In this way, the line of sight is partitioned into segments of the path inside the different disk components (assumed to be homogeneous) or the vacuum. For each part of the path, the exiting integrated intensity is calculated from the radiation transfer equation,

$$I = I_{\text{bg}} e^{-\tau} + S(1 - e^{-\tau}), \quad (\text{E1})$$

where I_{bg} is the integrated intensity calculated from the previous path segment (I_{bg} is taken as 0 for the first intersection); S is the source function of the component, I_{dust} or I_{cold} , or 0 for the vacuum; and τ is the optical depth, ∞ for the dust disk, 0 for the vacuum, and $\tau_0(l/R_{\text{out}})$ for a geometrical path l in the cold disk. The case of an intersection with the face of the flared disk is special, and the integrated intensity of the face, I_{face} , is added to the exiting intensity. Finally, when the total intensity is obtained, the dust continuum emission I_{dust} is subtracted if the line of sight intersects the dust disk.








Once the integrated intensity map is obtained, the model map to be compared with the observation is calculated as the convolution of the intensity map with a Gaussian beam equal to the synthesized beam of the observation.

E.3. Fitting Procedure

The fitting engine is the same as that used in Estalella (2017). The procedure samples the multidimensional parameter space using a Sobol pseudo-random sequence. For each sample, the model is computed, obtaining the integrated intensity map, the residual map, and the residual rms. The total number of samples of a fitting run is evenly distributed between a number of loops, a number of seeds, and a number of descendants for each seed. For the first loop, initial values and search ranges are assigned to the fit parameters, and the seeds of the parameter space within the ranges of each parameter are selected randomly around the initial values. For the next loops, the descendants of each seed are selected randomly in the parameter space around the seed. The descendants of all seeds for which the chi-square fit residual is lower are taken as seeds for the next loop, for which the search ranges are decreased by a constant factor. The procedure stops after the number of loops is completed.

The uncertainty in the values derived for the parameters is estimated as the increment of the parameters for which the chi-square residual does not exceed the minimum value by an amount $\Delta(m, \alpha)$, where m is the number of parameters fitted and α is the significance level (0.68 for a 1σ uncertainty). The value of $\Delta(m, \alpha)$ is given by a chi-square probability distribution with m degrees of freedom. For a more detailed description see Estalella (2017).

ORCID iDs

M. Fernández-López  <https://orcid.org/0000-0001-5811-0454>
 J. M. Girart  <https://orcid.org/0000-0002-3829-5591>
 J. A. López-Vázquez  <https://orcid.org/0000-0002-5845-8722>
 R. Estalella  <https://orcid.org/0000-0001-7341-8641>
 G. Busquet  <https://orcid.org/0000-0002-2189-6278>
 S. Curiel  <https://orcid.org/0000-0003-4576-0436>
 N. Añez-López  <https://orcid.org/0000-0002-3255-2665>

References

- Alves, F. O., Caselli, P., Girart, J. M., et al. 2019, *Sci*, **366**, 90
 Alves, F. O., Cleeves, L. I., Girart, J. M., et al. 2020, *ApJL*, **904**, L6
 Andrews, S. M. 2020, *ARA&A*, **58**, 483
 Añez-López, N., Osorio, M., Busquet, G., et al. 2020, *ApJ*, **888**, 41
 Bell, T. A., Cernicharo, J., Viti, S., et al. 2014, *A&A*, **564**, A114
 Beltrán, M. T., Cesaroni, R., Codella, C., et al. 2006, *Natur*, **443**, 427
 Beltrán, M. T., Cesaroni, R., Rivilla, V. M., et al. 2018, *A&A*, **615**, A141
 Beltrán, M. T., Rivilla, V. M., Cesaroni, R., et al. 2022, *A&A*, **659**, A81
 Beuther, H., Linz, H., Henning, T., Feng, S., & Teague, R. 2017, *A&A*, **605**, A61
 Busquet, G., Girart, J. M., Estalella, R., et al. 2019, *A&A*, **623**, L8
 Cantó, J., Curiel, S., & Martínez-Gómez, E. 2009, *A&A*, **501**, 1259
 Carrasco-González, C., Galván-Madrid, R., Anglada, G., et al. 2012, *ApJL*, **752**, L29
 Carrasco-González, C., Rodríguez, L. F., Anglada, G., et al. 2010, *Sci*, **330**, 1209
 Cesaroni, R., Sánchez-Monge, Á., Beltrán, M. T., et al. 2017, *A&A*, **602**, A59
 Cuello, N., Ménard, F., & Price, D. J. 2023, *EPJP*, **138**, 11
 Demidova, T. V., & Grinin, V. P. 2022, *ApJ*, **930**, 111
 Draine, B. T. 2006, *ApJ*, **636**, 1114
 Estalella, R. 2017, *PASP*, **129**, 025003
 Fernández-López, M., Curiel, S., Girart, J. M., et al. 2011a, *AJ*, **141**, 72
 Fernández-López, M., Girart, J. M., Curiel, S., et al. 2011b, *AJ*, **142**, 97
 Galli, D., & Shu, F. H. 1993, *ApJ*, **417**, 220
 Garufi, A., Podio, L., Codella, C., et al. 2022, *A&A*, **658**, A104
 Ginsburg, A., McGuire, B., Plambeck, R., et al. 2019, *ApJ*, **872**, 54
 Girart, J. M., Estalella, R., Fernández-López, M., et al. 2017, *ApJ*, **847**, 58
 Girart, J. M., Fernández-López, M., Li, Z. Y., et al. 2018, *ApJL*, **856**, L27
 Gómez, Y., Rodríguez, L. F., Girart, J. M., Garay, G., & Martí, J. 2003, *ApJ*, **597**, 414
 Gooch, R. 1995, in ASP Conf. Ser. 77, *Astronomical Data Analysis Software and Systems IV*, ed. R. A. Shaw, H. E. Payne, & J. J. E. Hayes (San Francisco, CA: ASP), 144
 Grant, S. L., Espaillat, C. C., Wendeborn, J., et al. 2021, *ApJ*, **913**, 123
 Guzmán Ccoolque, E., Fernández-López, M., Zapata, L. A., & Baug, T. 2022, *ApJ*, **937**, 51
 Haisch, K. E. J., Lada, E. A., & Lada, C. J. 2001, *ApJL*, **553**, L153
 Heathcote, S., Reipurth, B., & Raga, A. C. 1998, *AJ*, **116**, 1940
 Hernández-Hernández, V., Zapata, L., Kurtz, S., & Garay, G. 2014, *ApJ*, **786**, 38
 Hirota, T., Machida, M. N., Matsushita, Y., et al. 2017, *NatAs*, **1**, 0146
 Hsieh, C.-H., Lai, S.-P., Cheong, P.-I., et al. 2020, *ApJ*, **894**, 23
 Huang, J., Andrews, S. M., Öberg, K. I., et al. 2020, *ApJ*, **898**, 140
 Huang, J., Bergin, E. A., Öberg, K. I., et al. 2021, *ApJS*, **257**, 19
 Ilee, J. D., Cyganowski, C. J., Brogan, C. L., et al. 2018, *ApJL*, **869**, L24
 Jiménez-Serra, I., Báez-Rubio, A., Martín-Pintado, J., Zhang, Q., & Rivilla, V. M. 2020, *ApJL*, **897**, L33
 Joye, W. A., & Mandel, E. 2003, in ASP Conf. Ser. 295, *Astronomical Data Analysis Software and Systems XII*, ed. H. E. Payne, R. I. Jedrzejewski, & R. N. Hook (San Francisco, CA: ASP), 489
 Kauffmann, J., Bertoldi, F., Bourke, T. L., Evans, N. J. I., & Lee, C. W. 2008, *A&A*, **487**, 993
 Kurtovic, N. T., Pérez, L. M., Benisty, M., et al. 2018, *ApJL*, **869**, L44
 Le Gouellec, V. J. M., Hull, C. L. H., Maury, A. J., et al. 2019, *ApJ*, **885**, 106
 Liu, S.-Y., Su, Y.-N., Zinchenko, I., et al. 2020, *ApJ*, **904**, 181
 Louvet, F., Dougados, C., Cabrit, S., et al. 2018, *A&A*, **618**, A120
 Martí, J., Rodríguez, L. F., & Reipurth, B. 1993, *ApJ*, **416**, 208
 Masqué, J. M., Girart, J. M., Estalella, R., Rodríguez, L. F., & Beltrán, M. T. 2012, *ApJL*, **758**, L10
 Masqué, J. M., Rodríguez, L. F., Araudo, A., et al. 2015, *ApJ*, **814**, 44
 Maud, L. T., Cesaroni, R., Kumar, M. S. N., et al. 2019, *A&A*, **627**, L6
 McMullin, J. P., Waters, B., Schiebel, D., Young, W., & Golap, K. 2007, in ASP Conf. Ser. 376, *Astronomical Data Analysis Software and Systems XVI*, ed. R. A. Shaw, F. Hill, & D. J. Bell (San Francisco, CA: ASP), 127
 Mendoza, S., Tejada, E., & Nagel, E. 2009, *MNRAS*, **393**, 579
 Molinari, S., Noriega-Crespo, A., & Spinoglio, L. 2001, *ApJ*, **547**, 292
 Murillo, N. M., van Dishoeck, E. F., Hacar, A., Harsono, D., & Jørgensen, J. K. 2022, *A&A*, **658**, A53
 Öberg, K. I., Guzmán, V. V., Walsh, C., et al. 2021, *ApJS*, **257**, 1
 Ossenkopf, V., & Henning, T. 1994, *A&A*, **291**, 943
 Pineda, J. E., Arzoumanian, D., André, P., et al. 2023, in ASP Conf. Ser. 534, *Protostars and Planets VII*, ed. S. Inutsuka (San Francisco, CA: ASP), 233
 Pineda, J. E., Segura-Cox, D., Caselli, P., et al. 2020, *NatAs*, **4**, 1158
 Pinte, C., Teague, R., Flaherty, K., et al. 2023, in ASP Conf. Ser. 534, *Protostars and Planets VII*, ed. S. Inutsuka (San Francisco, CA: ASP), 645
 Plambeck, R. L., & Wright, M. C. H. 2016, *ApJ*, **833**, 219
 Remijan, A. J., Markwick-Kemper, A., & ALMA Working Group on Spectral Line Frequencies 2007, AAS Meeting, **211**, 132.11
 Robitaille, T. P., Tollerud, E. J., Greenfield, P., (Astropy Collaboration), et al. 2013, *A&A*, **558**, A33
 Rodríguez, L. F., & Reipurth, B. 1989, *RMxAA*, **17**, 59
 Rodríguez-Kamenetzky, A., Carrasco-González, C., Araudo, A., et al. 2017, *ApJ*, **851**, 16
 Rodríguez-Kamenetzky, A., Carrasco-González, C., González-Martín, O., et al. 2019, *MNRAS*, **482**, 4687
 Sakai, N., Sakai, T., Hirota, T., et al. 2014, *Natur*, **507**, 78
 Sánchez-Monge, Á., Cesaroni, R., Beltrán, M. T., et al. 2013, *A&A*, **552**, L10
 Tanaka, K. E. I., Zhang, Y., Hirota, T., et al. 2020, *ApJL*, **900**, L2
 Thieme, T. J., Lai, S.-P., Lin, S.-J., et al. 2022, *ApJ*, **925**, 32
 Ulrich, R. K. 1976, *ApJ*, **210**, 377
 van der Marel, N., Birnstiel, T., Garufi, A., et al. 2021, *AJ*, **161**, 33
 Vastel, C., Bottinelli, S., Caux, E., Glorian, J. M., & Boiziot, M. 2015, F2A-2015: Proc. of the Annual Meeting of the French Society of Astronomy and Astrophysics, ed. F. Martin et al., 313
 Williams, G. M., Cyganowski, C. J., Brogan, C. L., et al. 2022, *MNRAS*, **509**, 748
 Wilner, D. J., Wright, M. C. H., & Plambeck, R. L. 1994, *ApJ*, **422**, 642
 Wright, M., Bally, J., Hirota, T., et al. 2022, *ApJ*, **924**, 107
 Yen, H.-W., Gu, P.-G., Hirano, N., et al. 2019, *ApJ*, **880**, 69
 Yen, H.-W., Takakuwa, S., Ohashi, N., et al. 2014, *ApJ*, **793**, 1
 Zapata, L. A., Loinard, L., Rodríguez, L. F., et al. 2013, *ApJL*, **764**, L14
 Zapata, L. A., Rodríguez, L. F., Fernández-López, M., et al. 2020, *ApJ*, **896**, 132